Journal of Structural Geology 51 (2013) 206–225

Contents lists available at SciVerse ScienceDirect

Journal of Structural Geology

journal homepage: www.elsevier.com/locate/jsg

Shear zones in clay-rich fault gouge: A laboratory study of fabric development and evolution

Samuel H. Haines [a,*], Bryan Kaproth [a], Chris Marone [a], Demian Saffer [a], Ben van der Pluijm [b]

[a] The Pennsylvania State University, Department of Geosciences and Center for Geomechanics, Geofluids, and Geohazards, Deike Building, University Park, PA 16802, USA
[b] University of Michigan, Department of Earth & Environmental Sciences, 1100 N. University Ave, Ann Arbor, MI 48109, USA

ARTICLE INFO

Article history:
Received 10 March 2012
Received in revised form
31 December 2012
Accepted 9 January 2013
Available online 31 January 2013

Keywords:
Shear zone
Clay fabric
Riedel shear
Cataclasis
X-ray texture goniometry
Acoustic measurements

ABSTRACT

Clay-rich fault rocks have long been recognized to host distinctive fabric elements, and fault rock fabric is increasingly thought to play a fundamental role in fault mechanical behaviour in the brittle regime. Although the geometries of fabric elements in fault gouges have been described for almost a century, the genesis and evolution of these elements during shear, and their links to bulk mechanical properties, remain poorly understood. We characterize the development and evolution of fabric elements with increasing shear in a variety of clay-rich experimental gouges over shear strains of <1 to >20 and at normal stresses of 2–150 MPa in the double-direct shear configuration. In addition to SEM observations of experiment products at a variety of shear strains, we quantified clay fabric intensity and the degree of grain size reduction using X-ray Texture Goniometry (XTG) and particle size distribution (PSD) measurements. We also measured P- and S-wave velocities during shear to further probe the evolution of shear fabric and gouge properties. We find that clay fabric elements develop in a systematic manner regardless of the gouge material. Riedel shears in the R_1 orientation and boundary-parallel shears are the dominant fabric elements. Riedel shears nucleate at layer margins and propagate into the layer shortly after reaching yield stress. Clay particles rotate into the P-orientation shortly after Riedels propagate through the layer. The Riedel shears are through-going, but are $>10\times$ thinner than similar zones observed in coarser granular materials. Our results suggest that the weakness of clay-rich fault gouge may be less a function of anisotropic crystal structure, as has been suggested previously, and more a consequence of very thin shear surfaces permitting deformation in clay-rich materials with minimal dilation or cataclasis. The very thin shear surfaces are a function of the fine grain size of the materials and possibly polymodal PSD's.

1. Introduction and aims

The mechanical behaviour of geologic materials deforming in the brittle regime has been the subject of considerable interest for over a hundred years, owing to its role both in interpreting deformed rocks and in understanding seismic phenomena (e.g., Gilbert, 1884; Cloos, 1928; Riedel, 1929; Morgenstern and Tchalenko, 1967; Sibson, 1977; Byerlee, 1978; Crawford et al., 2008; Collettini et al., 2009, 2011). Experimental deformation of simulated gouge materials under controlled laboratory conditions has been one fruitful approach to investigate the frictional strength and stability of brittle faults, and the geometry of fabric elements with respect to shear (e.g., Dieterich, 1981; Anthony and Marone, 2005; Niemeijer and Spiers, 2007; Collettini et al., 2009; Haines et al., 2009; Niemeijer et al., 2010a,b; Ikari et al., 2011). Clay-rich gouges have garnered considerable recent interest, because they may explain the weakness of some natural faults (e.g., Wu et al., 1975; Wu, 1978; Wang et al., 1980; Shimamoto and Logan, 1981; Carpenter et al., 2011).

Outcrop and drilling studies document clay-rich gouge in many fault zones, and these outcrops commonly include consistent patterns of fabric elements. These faults are often dominated by a crude 'scaly' foliation (*sensu* Vannucchi et al., 2003) and phyllosilicate preferred orientation parallel to the 'P' orientation of Logan et al. (1979) (hereafter "P-foliation" – see Fig. 1) and through-going narrow shear surfaces parallel to the R_1 orientation of Logan et al. (1979) (e.g., Rutter et al., 1986; Chester and Logan, 1987; Erickson and Wiltschko, 1991; Cowan et al., 2003). These patterns of fabric elements are pervasive, fundamental features, and occur across

* Corresponding author. Present address: Chevron Energy Technology Corporation, 1500 Louisiana St., Houston, TX 77002, USA.
E-mail addresses: shhaines@umich.edu, faultgougeguy@gmail.com (S.H. Haines).

0191-8141/$ – see front matter © 2013 Elsevier Ltd. All rights reserved.
http://dx.doi.org/10.1016/j.jsg.2013.01.002

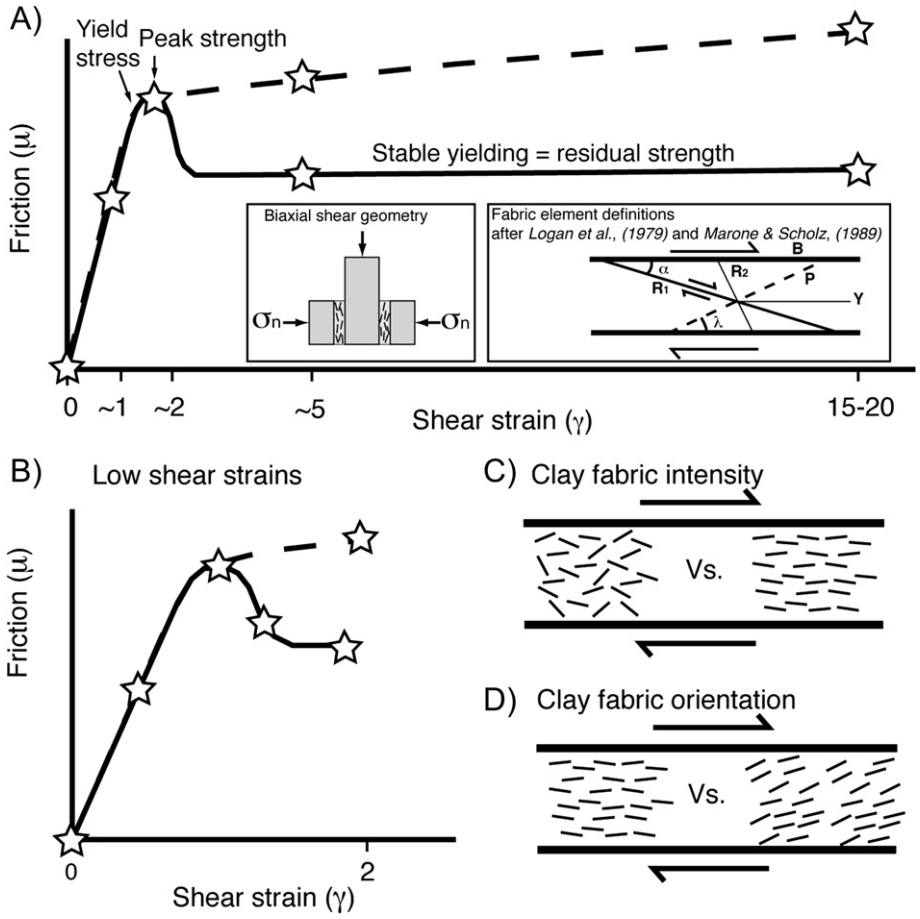

Fig. 1. Illustration of experiment plan used to understand fabric element evolution in this study. A) Stars are individual experiments stopped at particular points on stress-strain curves. Inset boxes show experimental configuration and terminology used for geometry of shear fabric elements of Logan et al. (1979) and Marone and Scholz (1989). B. Close-up of A) indicating region of multiple experiments at a given normal stress to understand the onset of Riedel shears. C) and D) Schematic depictions of phyllosilicate fabric intensity and fabric orientation as determined by XTG (X-Ray Texture Goniometry).

a wide range of conditions in both experimental and natural gouges (Fig. 1). Although studies of coarse-grained granular materials such as quartz, feldspars and carbonates (e.g., Logan et al., 1979; Marone and Scholz, 1989; Marone et al., 1990; Beeler et al., 1996) and experimental work specifically focused on phyllosilicate-rich materials have documented the evolution of similar fabric elements (e.g., Morgenstern and Tchalenko, 1967; Wijeyesekera and de Freitas, 1976; Maltman, 1977; Weber et al., 1978; Logan and Rauenzahn, 1987; Rutter et al., 1986; Arch et al., 1988; Logan et al., 1992; Saffer and Marone, 2003; Haines et al., 2009), the manner in which these elements evolve as a function of shear displacement, gouge mineralogy, particle morphology, and applied normal stress, as well as the associated changes in elastic properties, remains incompletely understood. The development and evolution of specific fabric elements, such as Riedel shears, and P-foliation, are also not well characterized.

Classic studies on fabric evolution in clay-rich materials date to the 1920's, but were conducted at significantly different conditions than those of modern friction experiments. These classic and systematic fabric evolution experiments were all conducted in the shear-box geometry common to soil mechanics (Morgenstern and Tchalenko, 1967; Tchalenko, 1968, 1970; Maltman, 1977, 1987; Naylor et al., 1986), which shears a relatively thick layer to low displacements and low shear strains at very low effective normal stresses <1 MPa. This approach also produces large gradients in the displacement magnitude across the layer.

Modern rock friction experiments, in contrast, employ one of three experimental configurations, the tri-axial 'saw-cut' configuration (e.g., Summers and Byerlee, 1977; Faulkner et al., 2010), the biaxial 'double-direct' configuration (e.g., Dieterich, 1981; Mair and Marone, 1999; Ikari and Saffer, 2011), or the ring-shear configuration (e.g., Beeler et al., 1996; Shimamoto and Tsutsumi, 1994; Niemeijer et al., 2010c). These configurations use much thinner layers and are sheared at higher normal stresses than the early shear-box experiments. Although shear-box experiments have compellingly reproduced the geometries of fault networks in the near surface and in the upper few km of the crust (e.g., Tchalenko, 1970; Naylor et al., 1986), their application to deeper tectonic faults, and comparison to modern experimental friction results, is problematic, owing to the different boundary conditions. The manner in which fabric elements develop in modern experimental configurations, which are more relevant to fault zone processes at higher stress and larger shear strains, remains surprisingly unclear.

Elastic wave velocities in granular materials are a function of the area and strength of grain contacts, stress across and between grains, and damage within grains (Sayers and Kachanov, 1995; Fortin et al., 2005), and therefore their measurement provides key insight into the evolution of these quantities during shear. Recent advances in experimental design have allowed quantification of elastic properties during shearing, by measuring ultrasonic wave speed across gouge layers (Knuth, 2011). Measurements of elastic wave velocities have been used to infer changes in microstructure

during deformation (e.g., Sayers and Kachanov, 1995; Schubnel et al., 2005; Fortin et al., 2005, 2007), but most measurements of elastic wave velocities during deformation have been made on intact sandstone or carbonate lithologies and only to the very low shear strains permissible in a triaxial apparatus.

Clay minerals have long been acknowledged to be frictionally weak relative to other common rock-forming minerals (e.g., Byerlee, 1978). Friction coefficients for clay minerals are typically reported as a single value (e.g., 'pure montmorillonite has a coefficient of friction of about 0.2', Scholz, 2002), yet recent work has documented substantial changes in frictional strength and behaviour of a given clay material based on physio-chemical changes, such as the presence of adsorbed water layers (saturation state) and normal stress (Saffer et al., 2001; Ikari et al., 2007, 2009). To date, the role of other variables, such as clay particle morphology, on frictional strength and frictional stability remains to be investigated. Most studies of frictional properties of clay-rich materials have been conducted on material that has then been crushed and sieved to silt-size or finer for experimental work (e.g., Moore et al., 1989; Ikari et al., 2007, 2009). Commonly, the resulting material has a platy morphology (Fig. 2). In contrast, clays extracted from natural fault gouges by settling in water, exhibit a more rounded morphology, reminiscent of crushed popcorn (Fig. 2). The effect of differing particle morphologies on materials of common composition remains to be investigated.

Here, we describe and quantify the development of fabric elements in clay-rich gouges subject to shearing in laboratory experiments under controlled normal stress and strain rate. We describe a suite of shearing experiments conducted on four different clay-rich materials: (1) silt-sized chlorite obtained by powdering a chlorite schist; (2) clay-sized chlorite separated from a natural low-angle normal fault gouge; (3) powdered illitic shale; and (4) powdered montmorillonite bentonite. For each material, we performed multiple experiments at a given effective normal stress, to a range of different shear strains. For each sheared layer, we characterized the fabric using a combination of SEM imaging and X-ray texture goniometry ('XTG', van der Pluijm et al., 1994) to quantify fabric intensity and orientation, and measured particle size distribution (PSD). To further understand the evolution of sheared layer properties and grain contacts with increasing shear strain, we also probed the layer elastic properties during shear by measuring P and S-wave velocity normal to the gouge layers (e.g., Knuth, 2011). We measured acoustic velocities for at least one high-strain experiment for each material.

2. Methods

2.1. Experimental materials

We studied three clay minerals that are common to natural fault rocks: illite, chlorite, and smectite (montmorillonite) (e.g., Wu, 1978; Haines and van der Pluijm, 2012). The illite was obtained by crushing commercially available illitic Rochester shale and sieving it to <106 μm. XRD analysis indicates the crushed shale consists primarily of illite with minor quartz and kaolinite. The montmorillonite is a commercially-available Ca-montmorillonite powder with a mean grain size of 83 μm (GSA Resources Inc., SM1502A); repeat XRD analyses indicate the montmorillonite is >97% pure. SEM observations show that the grains are not singe flakes of montmorillonite, but rather aggregates of sub-SEM scale

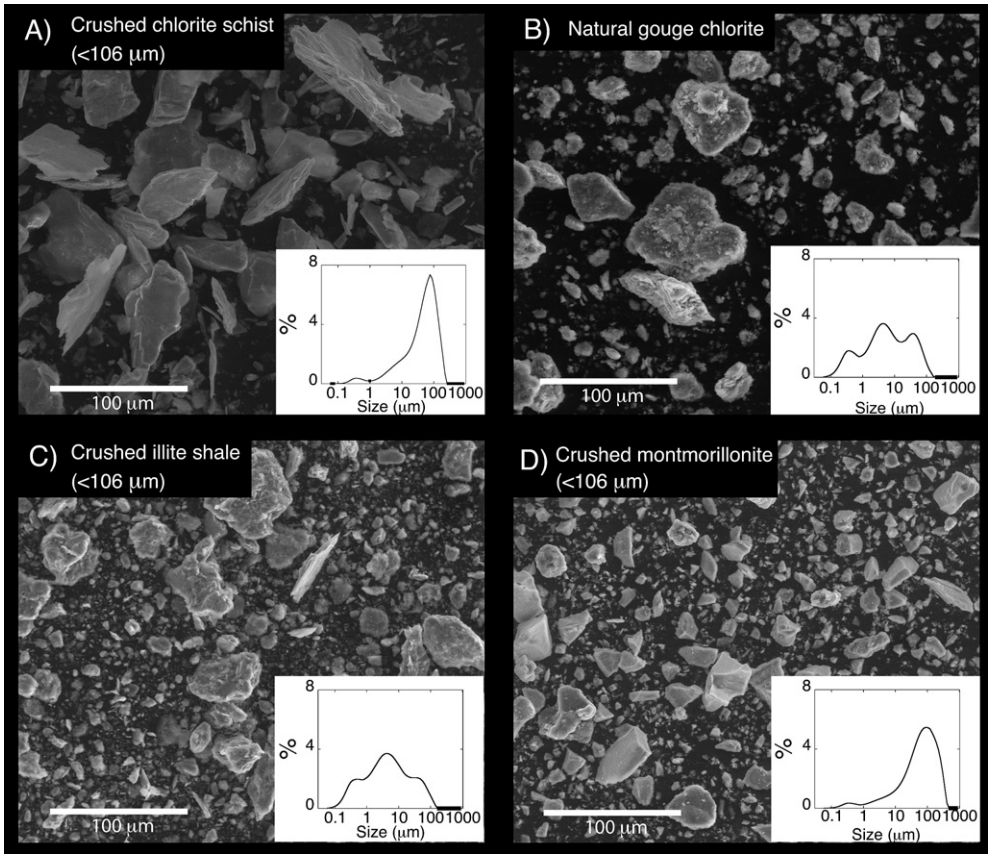

Fig. 2. SEM micrographs and particle-size distributions of initial materials used in all experiments. A) Crushed chlorite schist (<106 μm) B) Chlorite from gouge at the Mormon Point detachment, Death Valley, CA (<2 μm Stoke's equivalent). C) Crushed illite shale (<106 μm). D) GSA Resources Inc. montmorillonite SM1502A (<354 μm).

crystallites (Fig. 2). We estimate a crystallite size of 0.01 μm using the Scherrer equation, which relates XRD peak width to mean diffracting domain size (Moore and Reynolds, 1997).

Two different chlorites were used for this study, each with a distinct grain size distribution and particle morphology. The first chlorite was obtained from commercially available natural chlorite schist, which was crushed and sieved to <106 μm. XRD analysis indicates that the material is >97% chlorite, with traces of ilmenite and epidote. The second chlorite was obtained by separation in a water column from gouge obtained from an exposure of the Mormon Point Detachment in Death Valley, CA. The Mormon Point Detachment is an extensively studied, shallowly-dipping, NW-directed, low-angle normal fault of Miocene-to-Recent age (Pavlis et al., 1993; Miller, 1996; Cladouhos, 1999a, 1999b; Cowan, 1999; Cowan et al., 2003; Hayman, 2006; Haines and van der Pluijm, 2012). The detachment was sampled at 36°2′37″N, 116°44′12″W, where it juxtaposes poorly sorted Pliocene-Recent gravels in the hanging wall against fractured and chloritically metasomatized, mid-Miocene dioritic plutonic rocks in the footwall. The gouge is locally ~1 m thick at outcrop and is dominated by chlorite derived from the footwall (Haines and van der Pluijm, 2012). The chlorite in the gouge predates the brittle deformation, as it is compositionally and structurally indistinguishable from chlorite from the altered footwall, and contains P-foliation and rare R_1 shear fabrics. Chlorite was separated from the gouge by gravity settling in a water column to isolate the <2 μm (Stoke's equivalent) size fraction, which was then used for our friction experiments. The resulting material was gently disaggregated with a mortar and pestle in alcohol, and then sieved (Fig. 2). XRD analysis indicates the resulting gouge chlorite is >97% pure, and contains <5% interlayered smectite (Haines, 2008). This material is hereafter referred to as 'natural gouge chlorite'.

2.2. Shearing experiments

Experiments were conducted in the double direct shear geometry using a biaxial testing apparatus at room humidity and temperature (e.g., Saffer and Marone, 2003; Anthony and Marone, 2005). In this geometry, two gouge layers are sheared between three forcing blocks (Fig. 1). The side forcing blocks are held in place by applying a horizontal normal stress, which is maintained via servocontrol. The central block is driven between the side blocks at a controlled displacement rate, inducing shear within the gouge layers. The gouge layers were prepared using a levelling jig to produce a uniform frictional contact area (50 × 50 mm) and initial thickness (7 mm) prior to normal loading. Our gouge materials typically compressed to thicknesses of 1.5–2.5 mm under normal stresses (σ_n) of 2–150 MPa prior to shear. Both the centre and side blocks have roughened surfaces, which consist of triangular grooves 0.8 mm deep, which ensure slip within the gouge, rather than along the boundary of the layer (e.g., Mair and Marone, 1999). We measure the gouge shear strength during sliding at constant normal stress, and determine the coefficient of friction (μ) assuming zero cohesion. Friction measurements are made continuously as a function of shear displacement. During shear, the relative motion of the centre and side blocks causes geometric thinning (Scott et al., 1994). We correct for this effect in our calculation of shear strain. For our microstructural observations, we take samples from the centre of each layer to avoid boundary effects.

2.3. X-ray texture goniometry (XTG)

XTG clay fabric intensities were measured on a modified Enraf-Nonius CAD4 single crystal X-ray diffractometer in transmission mode using the method of van der Pluijm et al. (1994). The machine uses a molybdenum X-ray source operating at 15 mA and 35 kV and has a beam diameter of ~1 mm. XTG analysis for a gouge sample is a two-step process: first a 2Θ scan over the range 0.5–6.0° 2 Mo Kα (2–26° Cu Kα) identifies the (001) peaks of the clay phases in a sample. Then, a pole figure is collected for each of the principal (00l) peaks identified in the 2Θ scan. To collect a pole figure, the X-ray detector is first moved to the position that corresponds with the (00*l*) peak of the clay phase of interest: 7 Å for chlorite (002), 10 Å for illite (001), and 14 Å for smectite (001). The sample is then rotated both in its plane and about a vertical axis through a total of 1296 positions, measuring the intensity of that peak at each position with a count time of 2 s, covering roughly 65% of a full hemisphere. XTG thus measures the relative number of diffracting crystallites in the sample at each measured orientation. When the scan is complete, the pole figure of the diffracted beam is smoothed using a two-cycle smoothing process and contoured using multiples of a random distribution (MRD), which is analogous to percentage of the data per 1% area of the pole figure (Wenk, 1985). For example, an MRD value of 3.0 indicates that 3% of the total X-ray counts (after smoothing) are found within 1% of the area of the pole figure. Further details of the method are given in Haines et al. (2009) and data reduction in Day-Stirrat et al. (2011).

2.4. SEM and PSD measurements

Images were obtained on a FEI SEM operating at 20 kV in both backscatter electron (BSE) and secondary electron (SE) modes at low vacuum. Riedel shear orientations were measured graphically from printed SEM images from large wafers (>5 cm in length in the direction of shear). Particle size distribution (PSD) measurements were determined by laser obscuration (or light blocking) using a Malverin Mastersizer.

2.5. Elastic wave speed

For each material, we conducted at least one experiment with continual P- and S-wave measurements to high strain at normal stress of 50 MPa. S-waves were generated by a piezoelectric disk embedded in the right-hand side-block (500 kHz, lead-zirconate-titanate, 900 V pulse); P-waves were simultaneously generated by mode-conversion (for further details of the experimental configuration, see Knuth, 2011). The waves travel through the block assembly, sample the gouge layer, and are received at the left side-block by an identical piezoelectric disk. Waveforms are stacked – 100 per sample – and recorded every 2 s. We picked P- and S-wave arrivals by cross correlation. In general, our P-wave correlation coefficients are >0.90 and the S-wave correlation coefficients are >0.98. We then calculate velocities (Vp and Vs) from flight times and measured layer thickness. Measured velocities are highly precise (±<10 m/s), but have low accuracy, owing to the small sample thickness and potential errors in zero-time calibrations with the block assembly. The precisely measured relative changes in P and S flight times yield information about changes in elastic properties of the layer with progressive strain.

3. Results

3.1. Frictional strength

All four of the materials we studied exhibit distinct steady-state friction coefficients, which vary with normal stress (Fig. 3). Chlorite schist has a steady-state friction coefficient of $\mu = 0.29–0.33$ at normal stresses <20 MPa, and at normal stresses >20 MPa it work-hardens after the yield point, reaching values of $\mu = 0.48–0.52$ at shear strains near 20. In contrast, natural gouge chlorite is weaker than crushed chlorite schist, with values of μ decreasing from

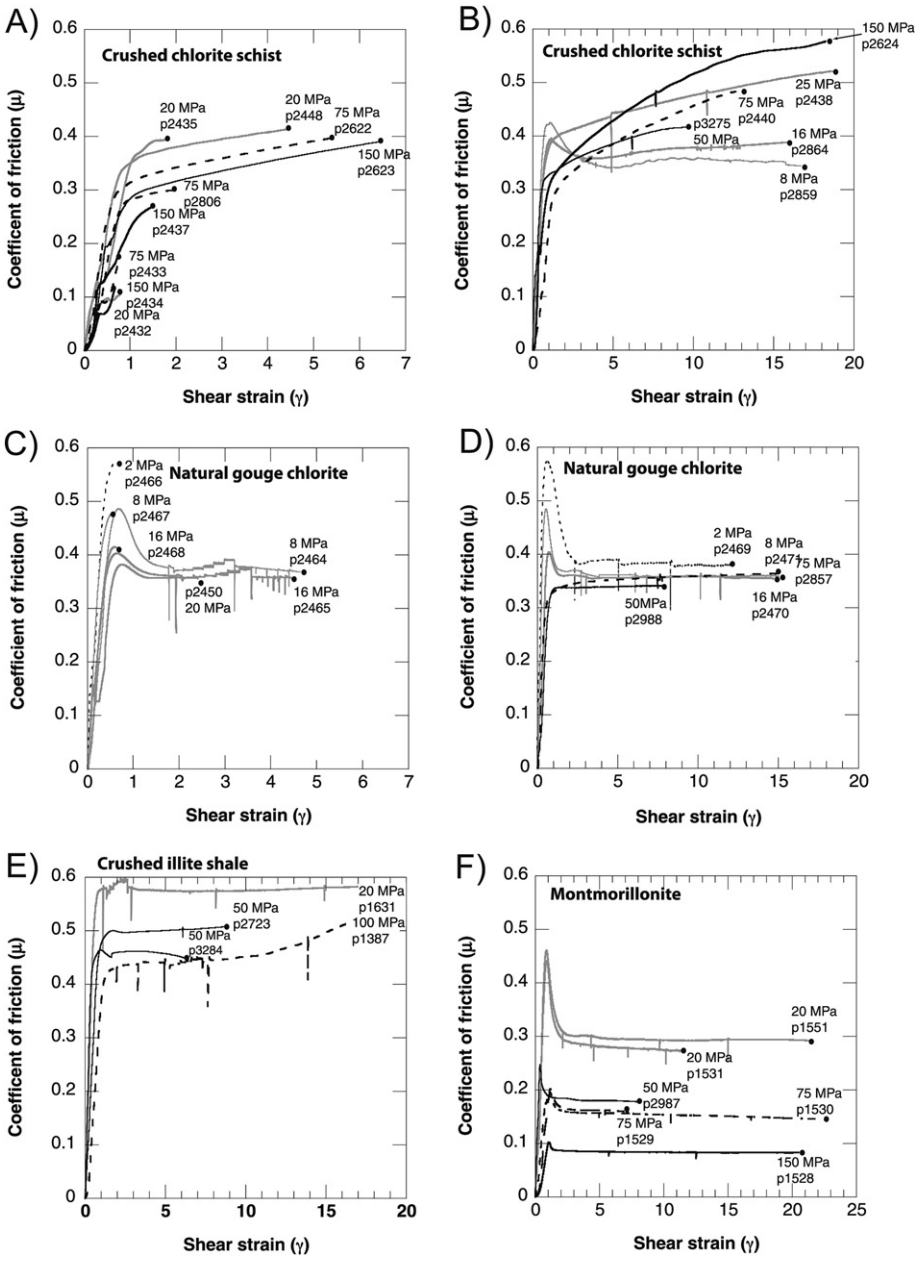

Fig. 3. Plots of coefficient of friction (μ) versus shear strain (γ) for experiments in this study. A) Crushed chlorite schist sheared to $\gamma < 6.6$ ($\sigma_n = 20$–150 MPa). B) Crushed chlorite schist sheared to $\gamma < 18.4$ at $\sigma_n = 8$–150 MPa. C) Natural gouge chlorite sheared at $\sigma_n = 2$–75 MPa. D) Natural gouge chlorite sheared to $\gamma < 4.9$. ($\sigma_n = 2$–20 MPa). E.) Crushed illite shale sheared at $\sigma_n = 20$–100 MPa. F) Montmorillonite sheared at $\sigma_n = 20$–150 MPa.

$\mu = 0.39$ at 2 MPa normal stress to $\mu = 0.30$ at 75 MPa. Illite is stronger than the chlorite, with $\mu = 0.60$ at 8 MPa normal stress and $\mu = 0.45$–0.50 at 50 MPa. At 100 MPa, the illite exhibits a friction coefficient of $\mu = 0.44$, but work-hardens at higher shear strains, reaching $\mu = 0.51$ at a shear strain of 16. The natural gouge chlorite strengthens with increasing sliding velocity, with the rate-dependent variable (a–b) ranging from +0.0002 to +0.006, similar to previously reported values for crushed chlorite schist reported by Ikari et al. (2011). The natural gouge chlorite strengthens only slightly with increasing hold times between sliding steps ($\Delta\mu$/decade = 0.008–0.01). The friction coefficient for montmorillonite decreases systematically with normal stress, consistent with previous work (Saffer et al., 2001; Saffer and Marone, 2003; Ikari et al., 2007). At 8 MPa normal stress, montmorillonite exhibits a steady-state friction coefficient of $\mu = 0.30$, decreasing to $\mu = 0.08$ at 150 MPa (Fig. 3). Our friction values are generally consistent with previous work on unsaturated clay minerals (e.g., Logan and Rauenzahn, 1987; Morrow et al., 1992; Saffer and Marone, 2003; Ikari et al., 2007), with the exception of the natural gouge chlorite, which is weak relative to previously published values (Byerlee, 1978).

3.2. Stress-strain behaviour

The stress-strain behaviour varies markedly between materials (Fig. 3). We observe three distinct types of behaviour: (1) Over-consolidated type behaviour, characterized by a pronounced peak strength and subsequent weakening with increasing shear strain ('rolling over'), until reaching a residual strength – as observed for montmorillonite at all normal stresses and for natural chlorite at $\sigma_n \leq 20$ MPa; (2) Plastic-type behaviour defined by a peak strength followed by continued yielding at the same stress – as observed for

illite shale at 8–100 MPa normal stress and in natural gouge chlorite at $\sigma_n \geq 50$ MPa; and (3) Strain-hardening behaviour in which strength increases throughout shearing ('work-hardening') – as observed in crushed chlorite schist at $\sigma_n \geq 20$ MPa and crushed illite shale at 100 MPa. The natural gouge chlorite also work-hardens slightly at 75 MPa, but the effect is far less pronounced. Some materials exhibit more than one type of behaviour. For example, at normal stresses of 8 and 16 MPa, crushed chlorite schist exhibits overconsolidated type behaviour at low strains, and a work-hardening trend at higher shear strains ($\gamma > 3$). At 100 MPa normal stress, illite exhibits plastic-type behaviour up to a shear strain of 7, after which a work-hardening trend develops.

For materials that exhibit overconsolidated type behaviour (i.e., montmorillonite, natural gouge chlorite and the crushed chlorite schist), the peak strength is most pronounced at low normal stresses, and is up to 1.5 times the residual strength (Fig. 3). The magnitude of the overconsolidation peak decreases systematically with increasing normal stress, but the range of normal stresses over which we observe a pronounced peak varies with the material (Fig. 4). Crushed chlorite schist only exhibits an overconsolidation peak at $\sigma_n < 20$ MPa, and natural gouge chlorite at $\sigma_n < 50$ MPa, whereas montmorillonite maintains an overconsolidation peak at all stresses we explored.

For all materials, at higher normal stresses, steady-state friction is reached at lower shear strains beyond the peak yield stress. To characterize these trends, we quantify the amount of shear strain required to reach steady-state after reaching the peak strength, relative to the shear strain from initial displacement to peak strength: $[(\gamma_{\text{onset of steady-state}} - \gamma_{\text{peak yield}})/(\gamma_{\text{peak yield}} - \gamma_{\text{initial}}]$. For example, in montmorillonite at 8 MPa this value is 4.9, at 20 MPa it is 3.7 and at 150 MPa it is 0.8 (Figs. 3 and 5).

The degree of work-hardening and its magnitude vary markedly by material, but both tend to increase at higher normal stresses. Work-hardening is absent in all materials at normal stresses of $\leq$8 MPa, and only the montmorillonite did not work-harden to some degree at normal stresses $\geq$75 MPa (Figs. 3 and 5). The normal stress at which we observe a transition from overconsolidated or plastic-type behaviours to work-hardening varies dramatically between materials (Fig. 5). For chlorite schist, work-hardening occurs at normal stresses $\geq$16 MPa, whereas natural gouge chlorite work-hardens only very slightly at 75 MPa, and crushed illite shale work-hardens only at 100 MPa. The work-hardening rates ($\Delta\mu/\Delta\gamma$) we observe are comparable to work-hardening rates reported for similar materials in triaxial configurations (Tembe et al., 2010).

3.3. Fabric evolution from SEM observations

3.3.1. Riedel shears

We observe a remarkably uniform sequence of fabric element development with shear strain in all of our experimental gouges. Experiments that were stopped before the yield stress lack visible fabric elements. However, clay particles are visibly aligned sub-parallel to the boundaries of the layer, which is likely a product of layer construction and normal loading prior to shear (Fig. 6a). Experiments stopped close to the peak stress contain shears in the R_1 orientation ('Riedel shears') that extend from the sideblock teeth only partway into the layer (Fig. 6b). B-shears are also observed that extend partially along the layer boundaries. We did not find incompletely-developed, isolated Riedels within the layer interior. Thus we conclude that Riedels nucleate at sideblock teeth and propagate into the layer (Figs. 6 and 7).

The first occurrence of through-going Riedel shears occur at the yield stress ($\gamma = 0.5-\sim2.0$), regardless of material. Experiments stopped just after the peak stress, and where the final increment of the stress-strain curve is either flat, indicating steady-state shear, or weakening, have one or more Riedel shears that extend completely across the layer (Fig. 7c), and a B-shear at least partially developed along one boundary. However, a regularly spaced network of Riedels is not developed at this point. In samples that are clearly past the peak stress, Riedel shears extend across the entire layer (Fig. 7d). At shear strains of $\gamma = 3$–4, a network of Riedels that extend across the layer is fully developed, along with a B-shear along one margin, if not both. At high shear strains ($\gamma > 10$), Riedel shears are present at lower angles with respect to the layer margins than those that formed at the yield point, and become sub-horizontal or even shallowly overturned with increasing shear strain (Fig. 6). By shear strains >15, these low-angle shear surfaces form an anastomosing network ranging from R_1 to Y or even P orientations – and multiple orientations are often visible on the same undulating surface. Notably, fractures and shears in the R_2 orientation, commonly observed in experiments in granular materials (e.g., Logan et al., 1979, 1992), are absent in all of our gouges. Slip surfaces parallel to the P or Y orientations are also absent, except at shear strains >15, when slip surface orientations become strongly undulatory.

We measured the angle of visible Riedel shears from SEM images of each experiment when possible. Although individual intact fragments of our sheared natural gouge chlorite could be extracted for XTG and SEM analysis, we did not obtain any fragments large enough (>5 cm length) for reliable measurement of Riedel

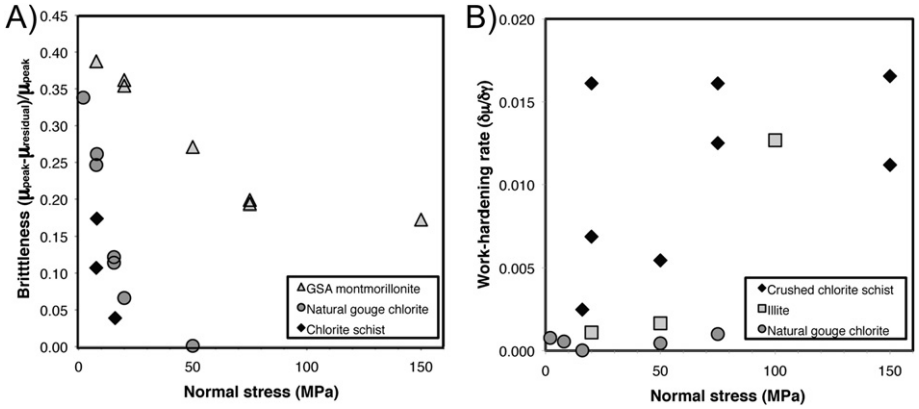

Fig. 4. A) A measure of brittleness (peak strength-residual strength)/peak strength for tests indicating overconsolidation (cf. Fig. 4C). Illite shale lacked overconsolidation peaks at all normal stresses studied and is not included. B) Work-hardening rate vs. normal stress for sample that exhibited work-hardening. Montmorillonite exhibited strain softening at all normal stresses studied and is not plotted.

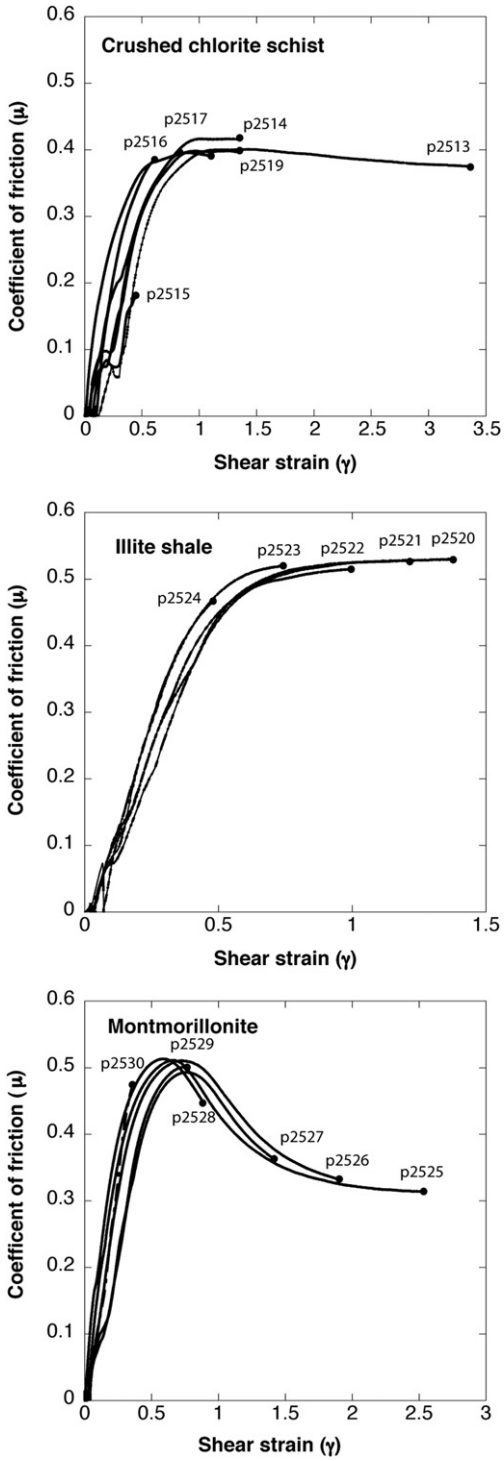

Fig. 5. Stress-strain curves for three gouge materials sheared at 8 MPa, 11 μm/s and varying shear strains. This series of tests was designed to document the initial formation of shear fabric.

orientations. Riedel shears that form at the yield stress are at higher angles for illite, (Riedel angle average = 13–17°, $\mu_{yield} = 0.39$) than those in crushed chlorite schist (Riedel angle average = 11–14°, $\mu_{yield} = 0.29$–0.39) and montmorillonite (Riedel angle range = 9–14°, $\mu_{yield} = 0.35$). These angles are roughly consistent with the frictional strength of the material at the time of initial Riedel formation, as predicted from Coulomb failure criteria (Logan et al., 1979) (Fig. 8).

In all of our experimental materials, the angle of Riedel shears decreases systematically with increasing shear strain (Fig. 8). For illite, average Riedel angles decrease from 13 to 17° at shear strains of 1–4, to 6–12° at shear strains of 5–12. For crushed chlorite schist, average Riedel angles drop from 11 to 14° at shear strains of 1–6, to 5–9° at shear strains of 8–20. For montmorillonite, average Riedel angles drop from 9 to 14° at shear strains of 1–5, to 6–10° at shear strains of 6–20. Scatter in the angle of Riedel shears also increases with increasing shear strain, because at high shear strain ($\gamma > 10$) Riedels are commonly undulatory, with some locally subhorizontal or even negatively sloping segments on a given slip surface (Fig. 6).

Riedel shear surfaces are consistently narrow and smooth, and the sheared samples tend to part along these structures when removed from the sample blocks (Fig. 9). In cross-section, Riedel shears are sharp, polished, planar surfaces, even after accommodating only limited overall layer shear strain. The margins of Riedel shear surfaces appear to consist of a <10 μm-thick layer of clay particles, often only one particle thick, aligned almost perfectly parallel to the surface. This thin boundary layer is generally very smooth (relief <1 μm). In plan view, slip-parallel striations are clearly visible and individual clay particles can clearly be seen pressed flat against the Riedel surface (Fig. 9). These zones of deformation along the margins of individual Riedels are <10–20 μm thick for all four materials. Individual clay flakes are commonly curved from the P to the R_1 orientation within <20 μm of the actual Riedel shear surface (Fig. 9). Although Riedel shears frequently extend entirely across the sheared layer with a length of up to a centimetre or more and visibly reflect light when optimally oriented in hand specimen (indicating a high degree of particle preferred orientation on the surface), the thickness of the domain of strong preferred orientation on a Riedel shear surface in these materials is only a few μm.

3.3.2. Phyllosilicate orientation from SEM observations

Owing to its coarse grain size relative to the other materials we studied, SEM images from the powdered chlorite schist samples provide the highest-quality images documenting the orientation of clay particles before and during shear. In the chlorite schist, the orientation of the phyllosilicate fabric changes with increasing shear. For experiments stopped before the peak stress and those stopped shortly thereafter ($\gamma < \sim 3$), where Riedel shears are incompletely propagated across the layer, the bulk phyllosilicate fabric is sub-parallel to the layer margins (the 'Y' orientation of Logan et al. (1979)). In this case, phyllosilicates within regions that are bounded by Riedels are rotated into the P orientation, whereas those in regions not transected by multiple Riedel shears remain in the Y orientation (Fig. 10). Once Riedel shears are fully developed, phyllosilicates are found in the P-orientation, even for the highest strain samples ($\gamma = 20$) in which the angle of Riedel shears has decreased. The crushed chlorite schist also exhibits grain size reduction with shearing: large grains (>~80 μm) are visible only up to shear strains of 2, beyond which the largest visible grain-size is ~50 μm.

3.4. Clay fabric intensity and orientation (XTG)

Fabric intensities vary markedly both between materials and as a function of shear strain (Fig. 11). In contrast to previous studies (Haines et al., 2009), we observe no systematic relationship between fabric intensity and normal stress (Fig. 12). The crushed chlorite schist has a very strong preferred orientation for samples subjected to simple compaction, ranging from MRD = 6.9 to MRD = 8.2. Fabric intensity decreases monotonically with increasing shear strain, decreasing to values of MRD = 4.7–5.8 at

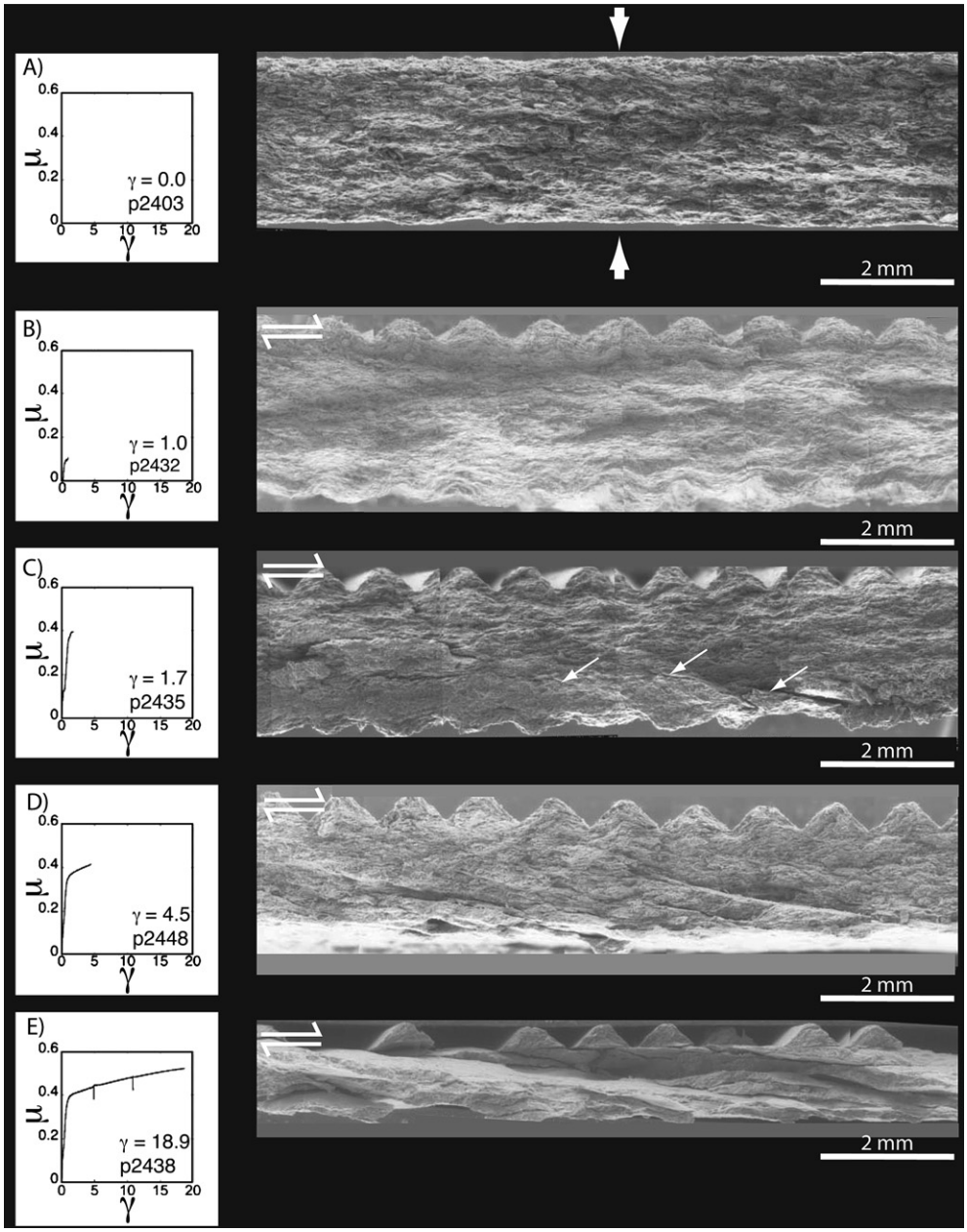

Fig. 6. SEM images of chlorite schist sheared at σ_n = 20 MPa and 11 μm/s to increasing shear strains. White arrows mark incipient R1 Riedel shears, which develop and become more prominent with increasing shear strain. Note that scale is the same in all images and that significant thinning has occurred by a shear strain of 19 (Panel E).

shear strains of ~20. Natural gouge chlorite was measured for comparison at 20 MPa, and crushed illite shale at 50 MPa. Natural gouge chlorite has significantly lower fabric intensity than the crushed chlorite schist, both prior to shearing (MRD = 4.4) and at a shear strain of 8.9 (MRD = 4.9). Crushed illite shale has relatively weak fabric intensity at a shear strain of 8.9 (MRD = 3.4). These results contrast with previous results published for montmorillonite sheared in the same experimental configuration (Haines et al., 2009), which have low fabric intensities (MRD = 1.7 at $\gamma = 0$, and MRD = 2.4–4.4 at $\gamma = >20$) and exhibit a slight sensitivity of fabric intensity to normal stress upon shearing, with slightly stronger fabric intensities observed at higher normal stresses (Fig. 11).

XTG fabric orientation rotates from layer margin-parallel ($\lambda = 0^\circ$) to $\lambda = 15$–35° towards the direction of shear ('P'-orientation) over shear strains from 0 to ~5, and then remains constant with further strain, for all of our materials (Fig. 12). Although there is considerable scatter in the measurements, the 20–35° angle of the P-fabric in the crushed chlorite schist is higher than the 10–33° measured from the montmorillonite samples in Haines et al. (2009) (Fig. 13), consistent with the frictional strengths of both materials, and with the idea that P fabric is oriented perpendicular to σ_1 (Logan et al., 1979; Haines et al., 2009).

The shape of the XTG pole distribution (Fig. 12) varies only slightly as a function of shear strain, with most samples having near-circular pole figures at low shear strains, and only slightly oblate pole figures at higher strains (>8), indicating some rotation of phyllosilicates about the Y axis of the strain ellipsoid. The obliquity of pole figures decreases with increasing shear strain, with montmorillonite having the weakest fabric intensities and

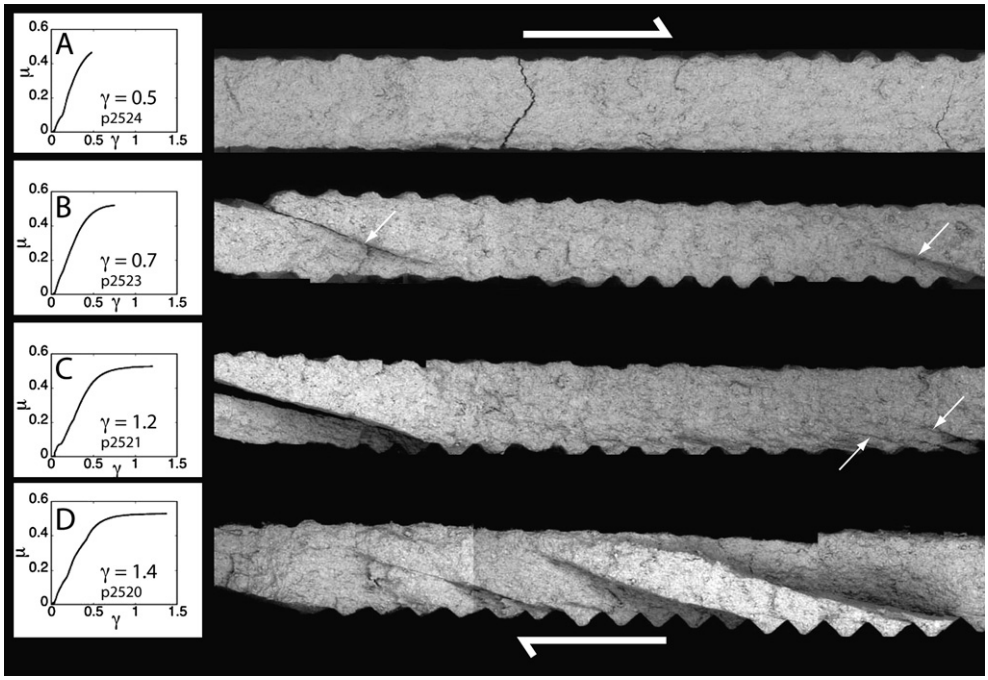

Fig. 7. SEM images of experiments on illite shale at 8 MPa and at various shear strains illustrating the development of fabric elements with increasing shear strain. Thin white arrows indicate incipient Riedel shears.

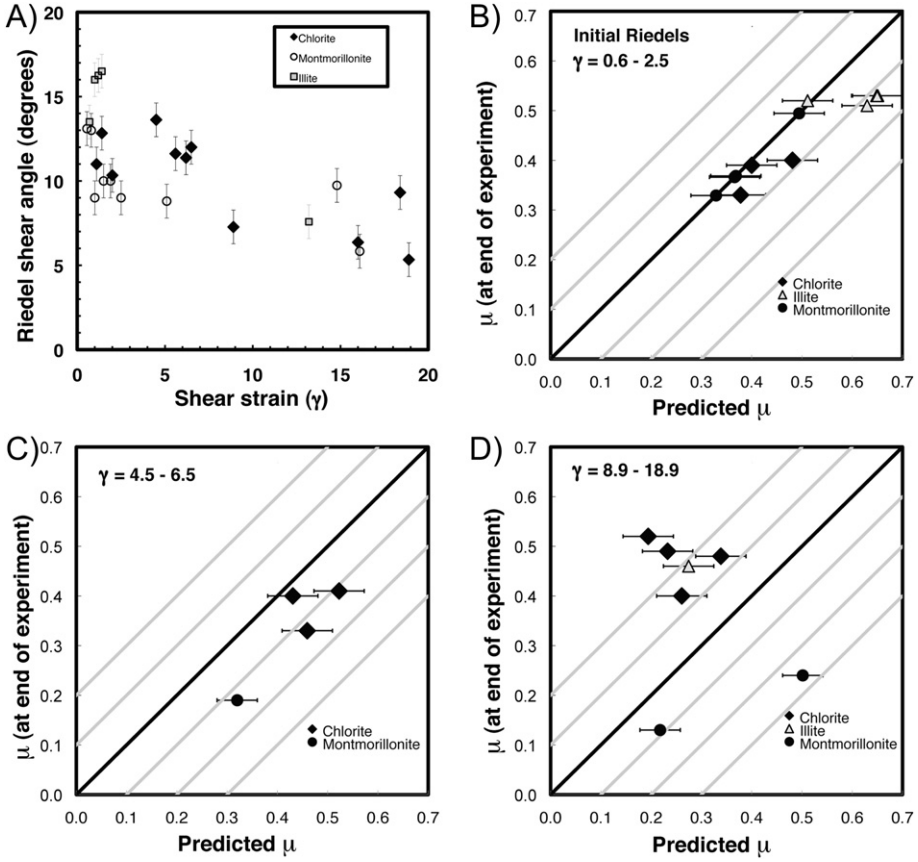

Fig. 8. Plots of Riedel shear angle (R_1 α) vs. shear strain as measured from SEM images. A) Angle of Riedel shear vs. shear strain for all materials. For following plots (B, C, D) coefficient of friction predicted from Riedel shear orientation vs. measured coefficient of friction at end of experiment. Black line is 1:1 line, each grey line is a deviation of 0.1 μ between μ predicted from measured angle and observed μ. B) Low shear strain ($\gamma = 0.6–2.5$). C) Medium shear strain ($\gamma = 4.5–6.5$). D) High shear strains ($\gamma = 8.9–18.9$).

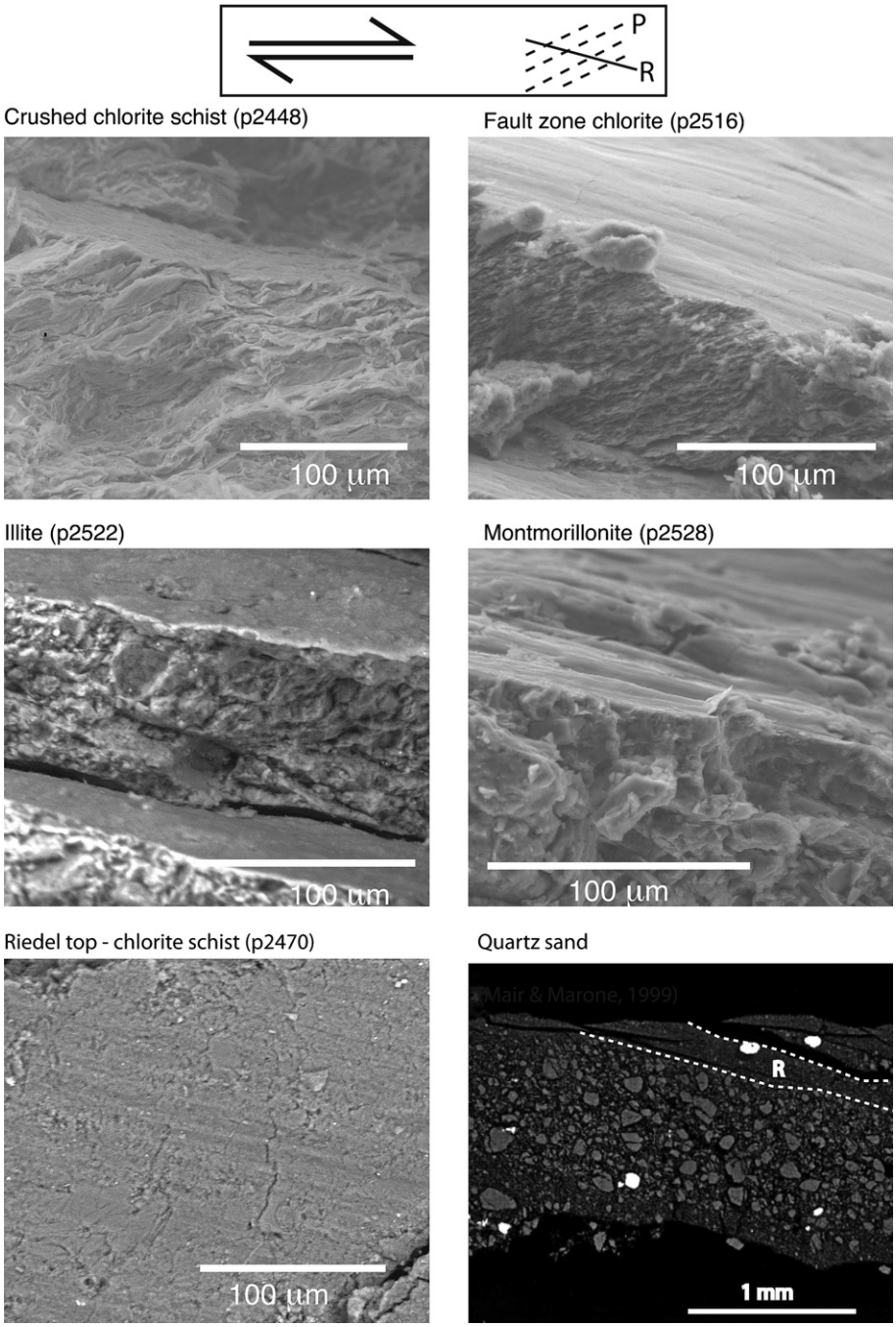

Fig. 9. SEM images showing Riedel shear surfaces in cross-section and oblique view. Sense of shear is top to the right in all images except chlorite schist, lower left panel, which shows plan view onto a Riedel shear surface in sheared natural gouge chlorite (p2470, $\gamma = 15.1$, $\sigma_n = 75$ MPa). Note striations on Riedel shear surface. Lower right: SEM image of Riedel shear from granular material (quartz sand, Mair and Marone, 1999). Note thickness of Riedel zone (R) relative to materials in this study.

most oblique pole figures, and the crushed chlorite schist with strong fabric intensity and near-circular pole figures. Natural gouge chlorite and crushed illite shale are both in between the end members defined by the crushed schist and montmorillonite. These pole figures are also more circular than those that are typically observed from natural fault rocks (Haines et al., 2009).

3.5. Particle size distribution (PSD)

Particle size distributions for all materials are shown in Fig. 14. Crushed chlorite schist and montmorillonite have asymmetrical, unimodal initial particle size distributions with modes at 76 μm for chlorite and 89 μm for montmorillonite. Both distributions have tails on the fine side of the mode ($d_{50} = 44–48$ μm and 58–61 μm respectively). By contrast, natural fault chlorite and crushed illite shale have initially trimodal grain size distributions with finer median grain sizes (natural gouge chlorite $d_{50} = 5–6$ μm, illite $d_{50} = 4$ μm). All distributions have apparent minima at 1 μm, which may be an artefact of the laser diffraction analytical technique (Storti and Balsamo, 2010). Illite and natural gouge chlorite generally do not exhibit grain-size reduction (or, comminution), whereas the chlorite and montmorillonite become finer-grained

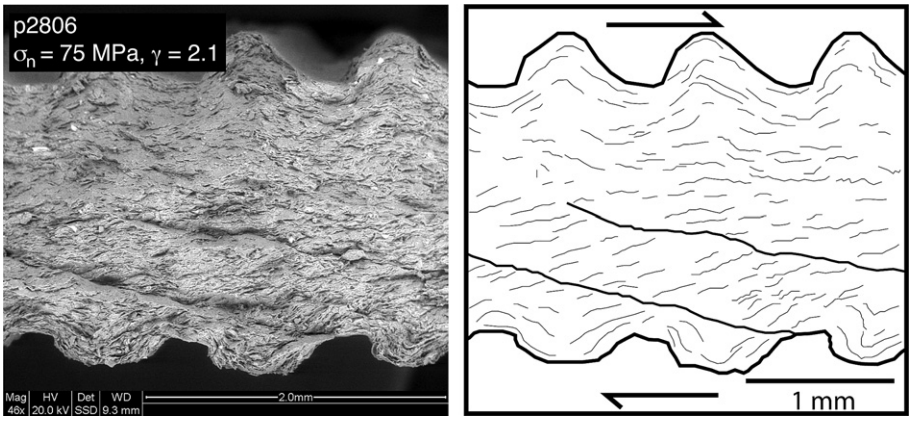

Fig. 10. Left: SEM image of experiment p2806 (sheared at $\sigma_n = 75$ MPa and to $\gamma = 2.1$) showing rotation of phyllosilicates within region bounded by Riedel shears and layer-parallel orientation outside of regions bounded by Riedel shears. Right: Line sketch of SEM image showing orientation of phyllosilicate packets within and outside of Riedel shear-bounded regions.

with increasing shear strain. Comminution in natural gouge chlorite occurs over the entire strain history, whereas for montmorillonite, comminution occurs predominantly at low strain ($\gamma < 1$) (Fig. 15). Increased normal stress leads to greater grain size reduction in the crushed chlorite schist, but has little effect on montmorillonite.

The particle size distributions of all materials are fractal over the grain size range 0.17 μm–66 μm (Fig. 15). Fractal dimensions vary markedly between materials and with shear strain, but are independent of normal stress. Crushed chlorite schist and montmorillonite both have low fractal dimensions (2.34–2.55) prior to shear, whereas natural gouge chlorite and crushed illite shale have relatively high fractal dimensions (2.84–2.97). Fractal dimension increases with increasing shear strain for the crushed chlorite schist, reaching 2.7 at shears strains of 20, but does not change significantly for the other materials (Fig. 15).

3.6. Elastic wave speed

All of our materials exhibit a trend of dramatic Vp and Vs increase from the beginning of shear to shortly after yield, $\gamma = \sim 0.5–1.0$ (Fig. 16), likely resulting from increased stress and thus increased contact area and strength between grains during load-up. Following yield, at shear strains of ~1.5–2.5, this trend changes and the rate of velocity increase slows markedly. For all materials except the chlorite schist velocities decrease following yield. With additional strain ($\gamma > \sim 2.5$), Vp and Vs increase again in the natural fault chlorite and crushed illite shale, whereas in the montmorillonite and crushed chlorite schist they remain nearly constant (Fig. 16).

4. Discussion

4.1. Fabric element evolution

The fabric elements developed in clay materials are consistent and subtly different from those developed in coarser-grained granular materials such as silt or sand-sized quartz, feldspars, carbonate minerals, or halite. Clay-rich materials develop a fabric dominated by 3 elements: (1) R_1 shears; (2) an orientation of clay particles parallel to the P-orientation in 'microlithons' between shear surfaces; and (3) B shears along the layer margins. The R_2

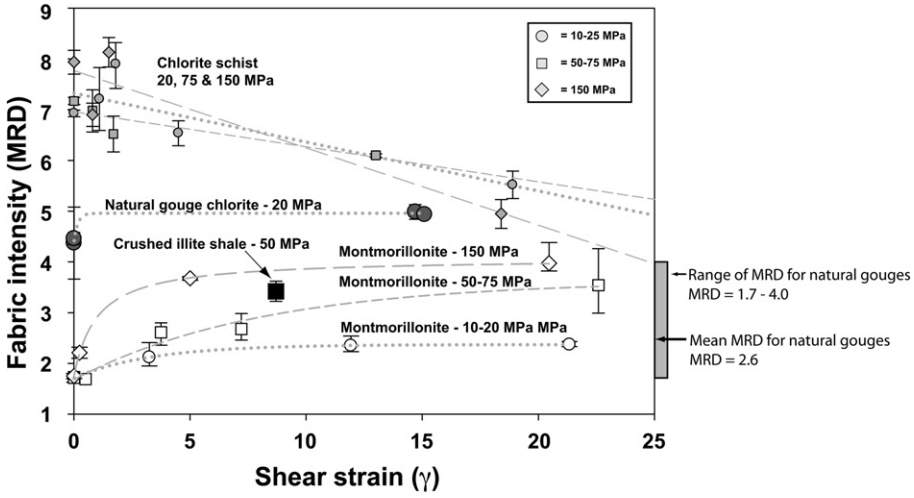

Fig. 11. Phyllosilicate fabric intensity measurements from XTG plotted against shear strain for materials used in this study. Upper and lower error bars are highest and lowest fabric intensity measurements from the same sample, with the symbol being the arithmetic mean of intensity measurements. Montmorillonite data and natural gouge ranges replotted from Haines et al. (2009). Dotted lines = regression for 10–25 MPa, short dash = 50–75 MPa, long dash = 150 MPa. Range of MRDs observed in natural gouges is taken from Haines et al. (2009).

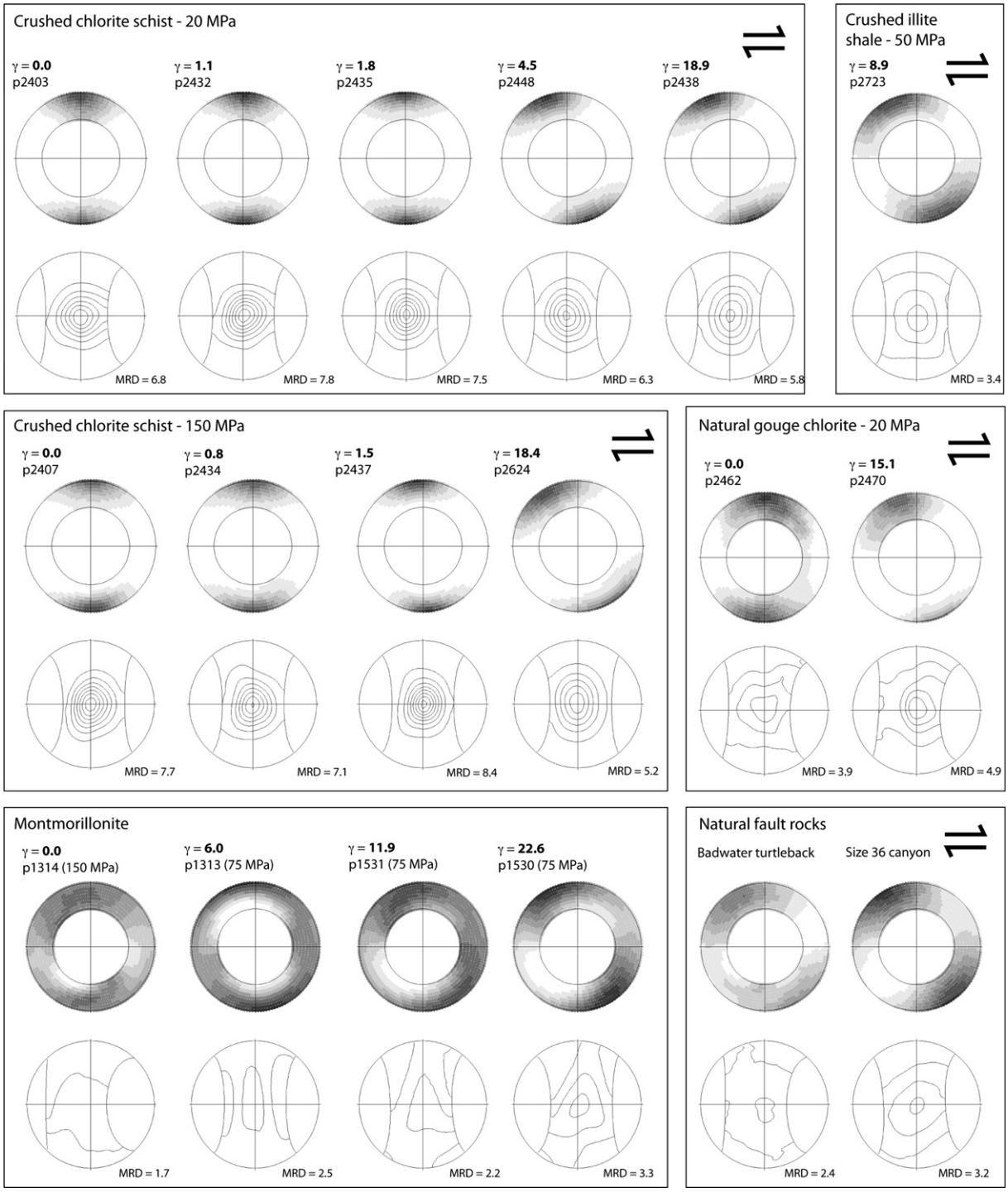

Fig. 12. XTG pole figure maxima orientation and XTG pole figure intensity data for experiments in this study. Each box contains data from a single material sheared at a single normal stress to increasing shear strains. Upper row for each box is fabric maxima orientation in the X–Z plane of the strain ellipsoid. Samples with strain of 0.0 have maxima parallel to the layer margin. Sense of shear in all plots in upper half of boxes is top to the right. Lower figures in each box are pole figures contoured in intervals of 1 MRD unit.

surfaces, common to coarser-grained granular materials under both natural and experimental conditions (Logan et al., 1979, 1992; Marone and Scholz, 1989), are absent in our gouges. Our observations are generally consistent with previous findings from clay-rich fault rocks and gouges (Morgenstern and Tchalenko, 1967; Rutter et al., 1986; Logan et al., 1992).

Fabric elements follow a consistent evolution with increasing shear strain, regardless of the dominant clay mineral or particle morphology (Figure 17). Riedel shears appear to develop at the layer margin just before reaching the yield stress, and propagate into the layer. Riedels first propagate completely across the layer just beyond the yield stress, and a pervasive network is developed by shear strains of ~3–4. As Riedels propagate across the layer, within regions of clay bounded by Riedels on either side ('microlithons'), clay platelets rotate towards the P orientation (Fig. 10). Once the Riedel network is fully developed, the material shows

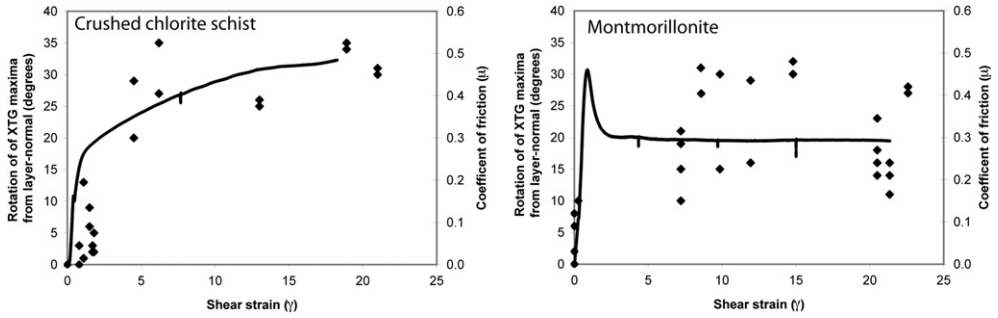

Fig. 13. Friction evolution and fabric rotation with shear strain. Rotation of the XTG pole maxima vs. shear strain for crushed chlorite schist (measurements from this study) and montmorillonite (measurements in Haines et al., 2009). A typical stress-strain curve is superimposed for each material. Chlorite schist = p2624 (σ_n = 150 MPa), Montmorillonite = p1551 (σ_n = 20 MPa).

steady-state behaviour with no new fabric elements forming. With continuing displacement, the orientation of clay particles within the microlithons remains constant in the P orientation even though Riedel shears continue to rotate to lower angles. This observation from XTG indicates that the microlithons are continuously deforming internally (frequently without significant cataclasis), permitting the phyllosilicate crystallites to remain perpendicular to σ_1 while they are simultaneously displaced along Riedels.

4.2. Mechanistic interpretation of stress-strain behaviour and fabric development

Before shear stress is applied to the layer, the gouge is compacted by the normal load. The initial (pre-shear) degree of preferred orientation of the particles is determined by the 'platyness' of the particle morphology and only minimally by the magnitude of the applied normal stress, as also observed in previous studies (Sintubin et al., 1995; Haines et al., 2009). From the onset of shear until yield, Vp and Vs increase systematically for all materials, consistent with strength increase as particles compact into tighter arrangements and the real area of contact increases (Fig. 16A, C, E and G).

The point at which Riedel shears nucleate on the layer margin and propagate into the layer coincides with a rollover in the stress-strain behaviour (Figs. 6C, 7B and C). We interpret this to reflect the onset of brittle failure and accommodation of displacement along localized shear surfaces. During this phase of shearing, the rate of Vp and Vs continues to increase for 0.1 to 0.7 shear strain units,

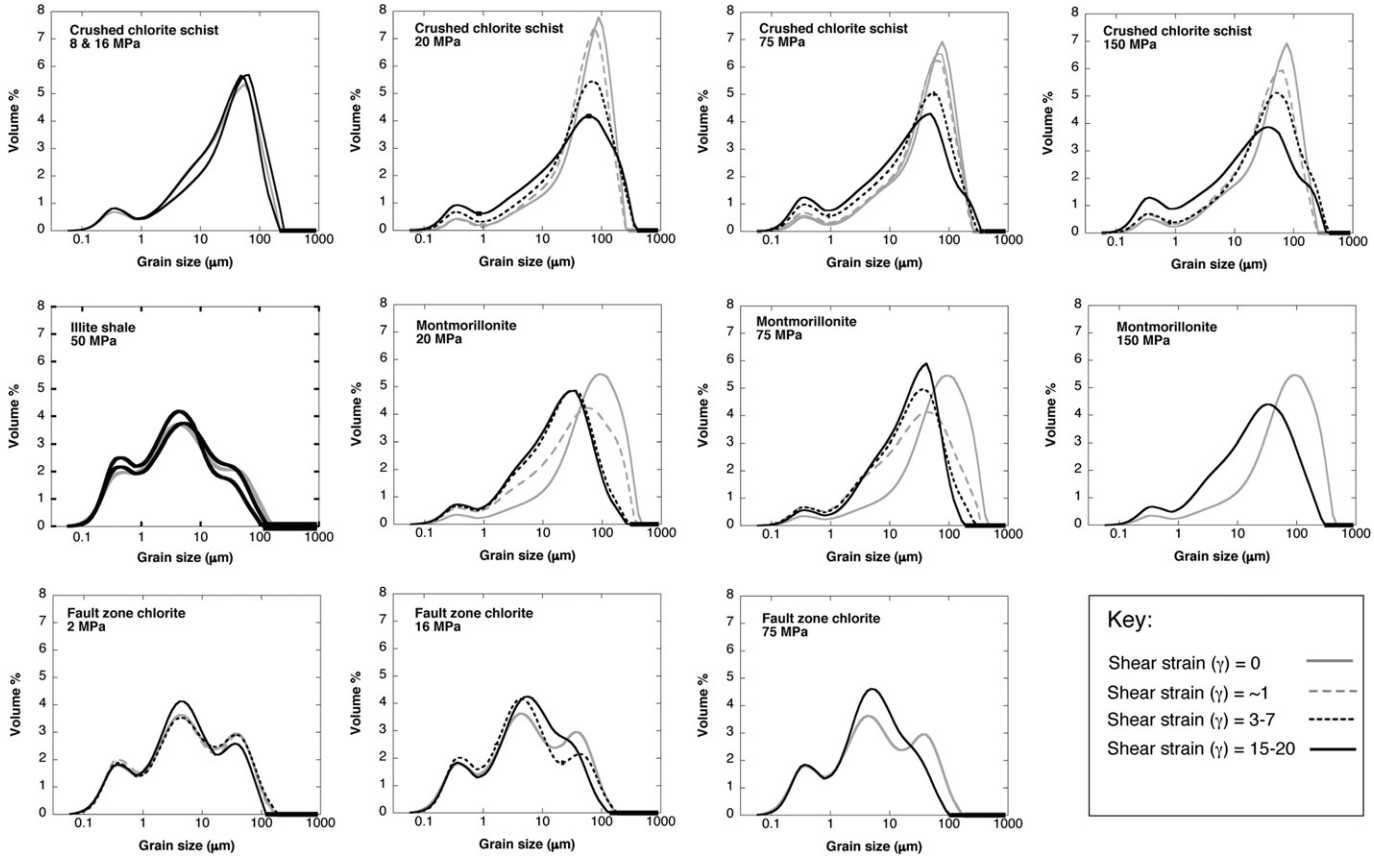

Fig. 14. Particle size distributions of experiments from this study as a function of shear strain.

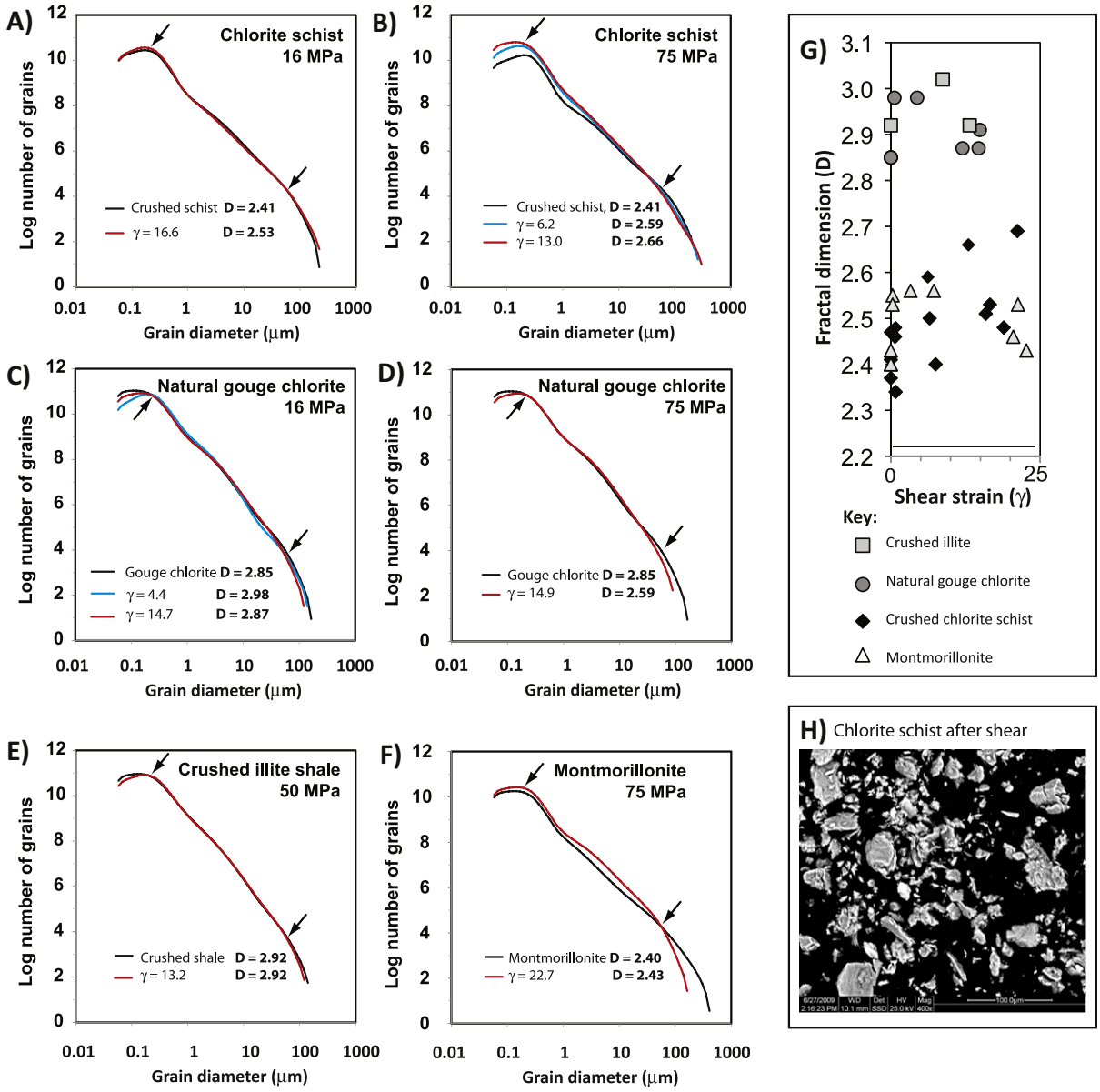

Fig. 15. Particle size distributions for samples post-shear. A–F) Representative plots for samples shown in Fig. 14. Arrows denote limits (~0.17–66 μm) used to determine best-fit line. The parameter D, fractal dimension, is the slope of the best fit line. G) Plot of D vs. shear strain for all materials shown in Fig. 14. H) SEM image of material from experiment p2440 after shear (crushed chlorite schist at 75 MPa, $y = 13.0$). Compare with Fig. 2A.

before decreasing (Fig. 16B, D, F and H). We interpret this change in wave speed trend to reflect a competition between velocity increase caused by a combination of layer compaction and in some cases (i.e., where we observe strain hardening behaviour) continued stress increase, and velocity decrease caused by formation of localized shear surfaces that disrupt force chains in the layer.

Beyond the yield stress, the first Riedel shears propagate entirely across the layer (Figs. 6D and 7C). At this point, Vp and Vs tend to decrease, consistent with a surface breaking the continuity within the gouge layer (Fig. 16B, D, F & H at point labelled '2'). Montmorillonite is the outlier; although Vp decreases as observed in the other materials, Vs remains constant. This disparity between Vp and Vs might be due to the onset of crack formation. In experiments on layered intact rock with Vp and Vs measured at multiple orientations, divergence between Vp and Vs has been interpreted to result from preferentially slowing of waves with an oscillation direction perpendicular to that of crack opening (Popp and Salzer, 2007). The rate of thinning of the layer decreases subtly in this stage of the experiments, consistent with opening of newly formed Riedel shears (Figs. 6 and 7).

A network of Riedels spanning the layer is developed at shear strains of 2–4, depending on the material (Figs. 6D and 7). The development of this network is coincident with Vp and Vs decrease (Fig. 16B, D, F and H, after '2'). Complete rotation of the clay particles to the P orientation occurs by a shear strain of ~5 (Fig. 12). Rotation of particles within microlithons is facilitated by the propagation of closely-spaced Riedel shears, as evidenced by rotation of phyllosilicates within Riedel-bounded packets and the preservation of initial layer-parallel orientation in regions that have not been cut by Riedels (Fig. 10). We suggest that once released by Riedel shears, phyllosilicate particles within microlithons are free to back-rotate to an orientation perpendicular to the maximum principal stress. Although the orientations of the principal stresses within the layer are impossible to determine directly in an anisotropic material such

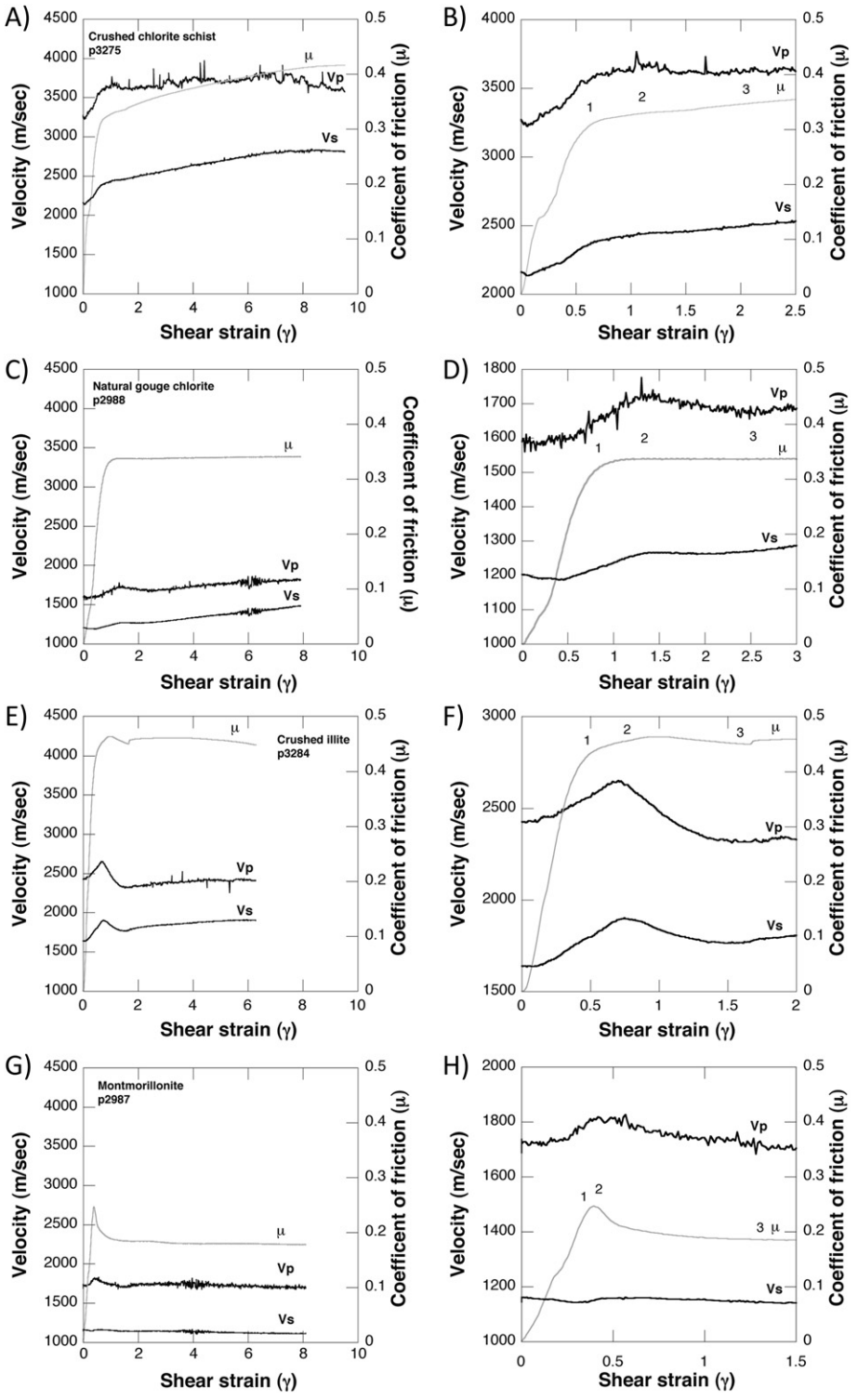

Fig. 16. A, B, C, E, G: P and S wave velocities with increasing shear strain from experiments on each material plotted together with stress-strain curve for the same experiment. All 4 experiments were conducted at $\sigma_n = 50$ MPa and sheared at 11 μm/s. B, D, F, H: Enlargements of the low shear strain regions of experiments in A, C, E, G, together with observations of Riedel shear formation from SEM images of other experiments in this study. 1 = Incipient Riedel shears; 2 = First Riedel shears across layer; 3 = Pervasive networks of Riedel shears across layer.

as ours, a maximum principal stress oriented at ~30° from the layer margin in the direction of shear is a mechanically viable explanation for the remarkably consistent back-rotation of phyllosilicate particles to the P orientation in both experimental materials and natural fault rocks (Figs. 10, 12 and 13, Haines et al., 2009).

At higher strains, the overall density of fabric elements does not change with strain, and P- and S-wave velocities remain nearly constant (Fig. 16A, C, E and G). However, the angular relationships of discrete fabric elements do continue to change. Similarly, the obliquity of the XTG pole figures observed at this range of shear

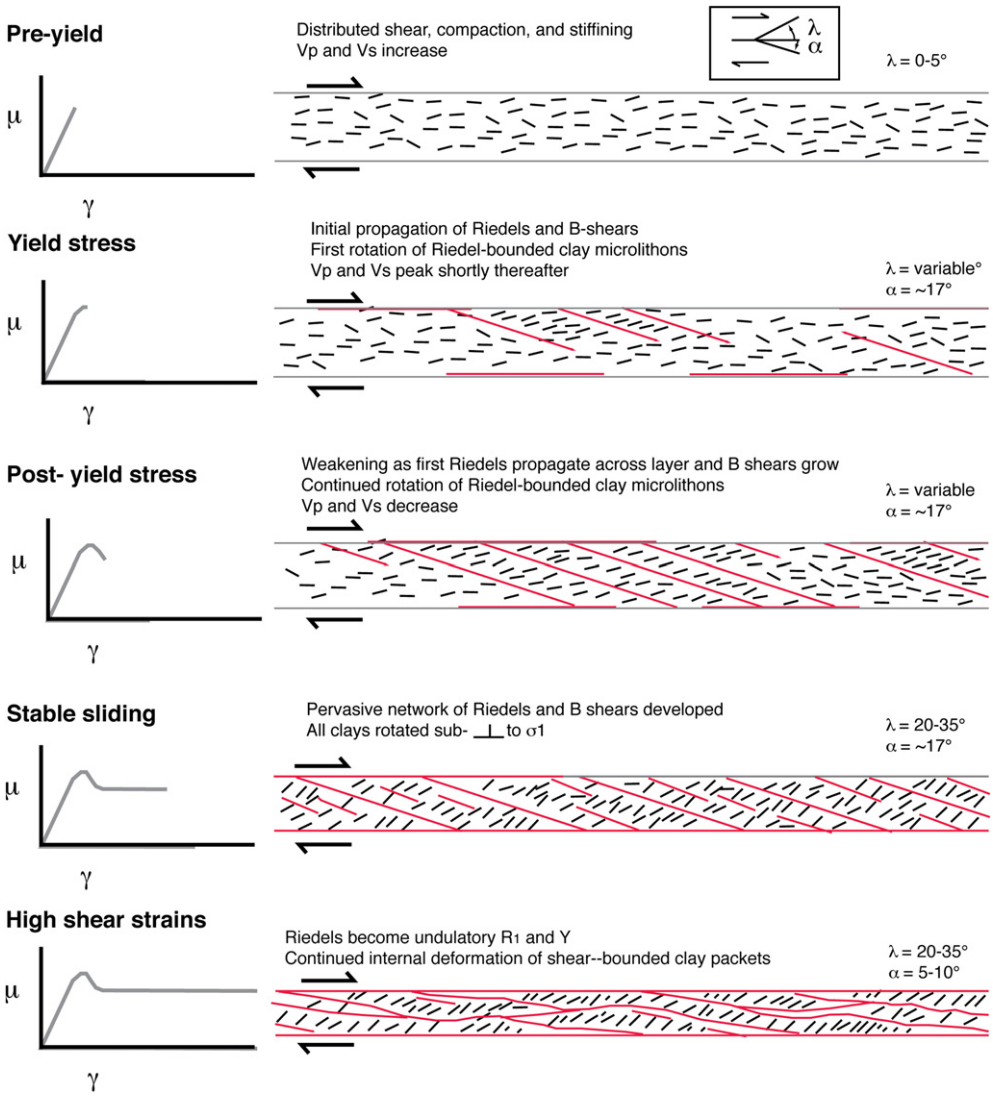

Fig. 17. Summary scenario showing evolution of fabric elements in clay-rich materials with increasing shear as obtained from results in this study. Red indicates surfaces that are interpreted to be active. (For interpretation of the references to colour in this figure legend, the reader is referred to the web version of this article.)

strains (Fig. 12) indicates a slight preferential rotation about the Y axis of the strain ellipsoid and is thus recording the variation in amounts of rotation of individual microlithons about the Y axis (perpendicular to shear). The obliquity is less apparent in the material with the strongest fabric intensity (crushed chlorite schist), owing to the far higher concentration of data points at the centre of the pole figures with strong fabric intensity (Fig. 12).

After propagation of Riedels across the layer, for materials composed of silt-sized single grains (crushed chlorite schist) or silt-sized aggregates of smaller grains (montmorillonite), continued shear is accompanied by cataclasis (or disaggregation of grain aggregates) in the microlithons (Fig. 14). Prior to Riedel formation, particles slide passively past each other. After Riedel formation, particles rotate and deform within the microlithons, causing significant grain-size reduction in some materials, as indicated by the PSD data (Fig. 14). Large angular particles become smaller and rounder, which we suggest promotes more efficient strain accommodation within the microlithons.

Vp and Vs increase slightly after Riedel propagation in the chlorite schist, and remain constant for the montmorillonite (Fig. 16). We suggest that the wave speeds respond to two competing processes during deformation of the layer: 1) the progressive loss of porosity and increase in the overall number of grain contacts causing velocity to increase (Fortin et al., 2005), and 2) microcracking within grains causing velocity to decrease, sometimes by a factor of two from the initial (i.e., pre-shear) velocity in intact rock (Sayers and Kachanov, 1995; Schubnel et al., 2005). A third potential process is the continuously increasing load in work-hardening material (i.e., the chlorite schist) that may cause an additional velocity increase. We do not see a strong grain microcracking signature in our experiments, as we observe either an increase in Vp and Vs relative to pre-shear Vp and Vs (as for all materials except for montmorillonite) or no change in Vp and Vs relative to pre-shear values, as with the montmorillonite. We suggest that the first (porosity loss) and third (load) processes are probably most important in the materials we studied, as our granular materials are different from the intact rock used by Sayers and Kachanov (1995) and Schubnel et al. (2005) in which microcracking dominated. The crushed chlorite schist exhibits a small velocity increase, consistent with both strength increase and grain crushing; montmorillonite exhibits no increase, perhaps reflecting steady strength and limited grain crushing at high

strain. For materials composed predominantly of clay-sized particles (natural gouge chlorite and crushed illite shale), Vp and Vs resume a slow increase after the network of Riedels has propagated across the layer (Fig. 16). This suggests a gradually strengthening granular framework owing to compaction within the microlithons, but a lack of significant cataclasis (middle left and bottom 3 panels of Fig. 16).

For all materials, Riedel shears gradually lengthen and rotate to lower angles with increasing shear strain (Fig. 8A), while microlithons compact and deform both in a cataclastic and ductile manner to maintain a P orientation that is crudely sensitive to the angle of internal friction of the material (Fig. 13). The relative predominance of plastic versus brittle deformation evident in Fig. 3, for otherwise compositionally-identical crushed chlorite schist and natural gouge chlorite, indicates that the style of deformation is controlled by grain morphology, and perhaps by grain size and grain size distribution. The relative importance of these processes is, however, not clear from our dataset.

4.3. Riedel shear angles and principal stresses

Riedel shear angles have been suggested to reflect the effective coefficient of friction of fault zones (Logan et al., 1979; Moore et al., 1989). Our data indicate that this assumption is only valid at the time of first Riedel formation (Fig. 8B), as the orientation of Riedel shears progressively decreases with increasing shear strain (Fig. 8A), whereas the coefficient of friction reaches a constant residual value (Fig. 2). As a result, the value of μ in our sheared layers predicted from Riedel orientations is far different from the friction coefficients we measure at shear strains beyond the yield stress (Fig. 8C and D). The difference between predicted frictional strength vs. actual frictional strength varies strongly with material, especially at high shear strains (Fig. 8D).

For crushed chlorite schist and crushed illite shale, measured coefficients of friction at the end of the experiment are far higher than coefficients of friction calculated from Riedel angles ($\mu_{actual} - \mu_{predicted} = 0.1–0.3$), whereas for montmorillonite they are lower ($\mu_{actual} - \mu_{predicted} = -0.1$ to -0.2). This difference in behaviour between materials is attributed to particle morphology. All materials studied have a near-uniform tendency for Riedel angles to decrease with increasing shear strain. Crushed chlorite schist samples strongly work harden. This work-hardening has the effect of increasing the real coefficient of friction in the material after Riedel formation at a rate far greater than the rate at which the Riedel angle decreases. Illite maintains a constant friction after yield stress, but the Riedel angle also decreases with increasing shear strain, resulting in a smaller discrepancy between the two values. Montmorillonite, on the other hand, weakens after the peak stress, reaching a steady-state residual friction significantly lower than the peak value.

Our measurements support the idea that Riedel shears initiate as Coulomb fractures, but evolve with increasing shear strain to orientations that are independent of the material's internal friction angle. Our data also indicate that the use of Riedel angles to estimate the angle of internal friction of a material is unreliable, unless the strain history of the material is very well known. In comparison, our XTG data suggest that the microlithons may be more faithful recorders of the orientation of the principal stresses than Riedel surfaces. Because the orientation of phyllosilicate basal planes in the microlithons remains parallel to the P orientation, (despite the rotation of the Riedels to progressively lower angles with increasing shear strain) the microlithons must continue to deform and rotate after the formation of through-going Riedel surfaces so that the crystallites in the P orientation can remain perpendicular to the likely σ_1 direction.

4.4. Mechanisms for the frictional weakness of clay gouges

The frictional weakness of clay minerals relative to other rock-forming minerals has generally been explained in terms of crystal structure and chemistry (e.g., Summers and Byerlee, 1977; Morrow et al., 2000). Relatively weak (001) interlayer bonds in phyllosilicates means that bonds in clays can be broken much more easily than in most other rock-forming minerals, and thus facilitate slip (e.g., Wu, 1978; Moore and Lockner, 2004). In addition, the presence of weakly-bonded adsorbed water layers in clays (especially smectites and vermiculites) further enhances the weakness of swelling clays by creating a 'pseudo' pore pressure effect as interlayer water molecules are pressed out at higher stresses (e.g., Wu, 1978; Bird, 1984; Colten-Bradley, 1987; Ikari et al., 2007). Our experiments indicate that minimal cataclasis occurs in clay-rich materials from natural faults and within synthetic gouges with similar grain size distributions, even when sheared at relatively high normal stresses (Fig. 14). This observation suggests that frictional weakness due to the weakness of bonds is an unlikely explanation, because there is little or no grain breakage. In comparison, compositionally identical, coarser-grained materials (e.g., crushed chlorite schist) exhibit far more grain breakage under the same stress conditions.

We suggest that a combination of fine grain size, particle morphology and a polymodal grain size distribution allow sheared clay to deform by ductile flow of particles within the microlithons, probably by grain boundary sliding, and without dilation or grain breakage. Our observations also suggest that relatively thin Riedel shear zones (relative to those found in coarser-grained granular materials), and possibly polymodal size distributions facilitate unusual frictional weakness in clays. Riedels in clay-rich layers have far less surface area than Riedel surfaces or zones in granular layers, and so must require far less energy to displace particles along discrete surfaces, rather than in the 10's–100's of μm thick zones of distributed comminution common to granular layers (e.g., Marone and Scholz, 1989; Mair and Marone, 1999; Fig. 9).

The observation that phyllosilicate-rich materials rapidly localize deformation onto thin surfaces (several orders of magnitude thinner than zones of similar orientation found in coarser-granular materials) indicates that the development of sharp, polished, through-going surfaces early in the displacement history plays a key role in reducing the macroscopically measured frictional strength of clay-rich gouges. In many of our materials, SEM observations indicate cataclasis occurs on Riedel surfaces alone and not elsewhere in the material, suggesting that cataclasis is occurring only in the very small fraction of the total gouge volume occupied by Riedel surfaces, thus requiring less energy than the more pervasive cataclasis in coarser-grained materials. Because the Riedel surfaces in clays are far thinner than those that form in granular layers, and yet play a profound role in controlling macroscopic frictional properties, it is likely that the location and continuity of phyllosilicates will control the overall frictional behaviour of mixed-phase layers, perhaps more so than their bulk abundance (Schleicher et al., 2006, 2010; Collettini et al., 2009).

Anthony and Marone (2005) demonstrated that particle roughness significantly increased frictional strength for sand-sized quartz, and it is apparent that the same process is applicable to clays. Platy grains require more energy to deform internally within microlithons, requiring cataclasis, whereas the more rounded grains of the natural gouge chlorite require less energy to deform. Although natural gouge clay grains are less anisotropic than are commonly depicted (Fig. 2), they still possess some anisotropy that responds to the principal stress and aligns along the P orientation. The degree of this preferred orientation measured by XTG correlates inversely with the apparent roundness of the particles.

The fine grain size of clays must also play a role in their frictional weakness relative to coarser-grained equivalents. As Riedel shears are common to both coarse- and fine-grained materials, the nature of deformation within the microlithons must play a significant role. We suggest that the combination of finer grain size and polymodal grain size distribution in the natural gouge chlorite and crushed illite shale facilitates the ductile deformation required to maintain the consistent orientation of the clay fabric in microlithons while the bounding Riedel shears rotate. Ductile deformation of silt-sized grains requires comminution, and thus additional energy, but deformation of clay-sized grains with natural morphologies may not.

4.5. Implications for analogue experiments

The dramatic difference in frictional strength between the two chlorite materials with similar stress and strain histories indicates that grain size and particle morphology play a significant role in frictional strength of sheared material, and that fault gouge mineral composition is not the only factor to consider. The crushed chlorite schist is a poor analogue for chlorite in natural faults; its frictional properties are very different from the natural gouge chlorite, likely owing to the fact that the grain size distribution and particle morphologies differ from material in natural gouges (c.f. Fig. 2). In contrast, the crushed illite shale is probably a good analogue for natural illitic gouges, because the grain size distribution is polymodal and fine-grained, and similar to that found in natural gouges. The fabric intensity upon shearing is also similar to natural gouges (Haines et al., 2009). These results highlight the role of grain size and particle morphology on friction, and have significant implications for friction experiments commonly used to simulate shearing processes in natural fault zones, but which have focused primarily on variations in gouge composition. In particular, our work indicates that careful characterization of particle size and shape in analogue materials is essential.

4.6. Implications for permeability of experimental and natural gouges

Our findings may have implications for the permeability and permeability anisotropy of both natural and synthetic clay-rich gouges (Morrow et al., 1984; Brown et al., 1994; Takahashi et al., 2007; Faulkner and Rutter, 1998). The permeability anisotropy observed in some clay-rich gouges has been explained variously as a function of either a) cataclasis decreasing permeability by increasing the number of fine grains relative to coarse grains and blocking pore throats (Morrow et al., 1984; Takahashi et al., 2007) b) development of fabric elements during shear (Brown et al., 1994) or c) interlayered porous clastic layers often found in natural gouges (Faulkner and Rutter, 1998; Faulkner et al., 2010). Most experiments that document permeability anisotropy in sheared clay-rich materials both lack coarse granular components, and still observe layer-normal permeability reductions of 1–3 orders of magnitude with shear. Permeability anisotropy can thus occur simply as a function of shear and does not require compositional variations in the gouge (Faulkner et al., 2010). Our SEM observations of very thin Riedel surfaces with strong preferred phyllosilicate orientation, compared with the relatively weak XTG-measured fabrics within microlithons, suggest that Riedel shear surfaces could act as barriers to fluid flow across the layer. Measurements of permeability with increasing shear strain on saturated gouges using identical experimental configuration and the same illite used in our experiments have reported permeability reductions of 1–3 orders of magnitude over shear strains from $\gamma = 0$–20 (Ikari et al., 2009). Furthermore, these experiments showed that the most pronounced reduction in permeability occurs by shear strains of <5, over the same strain interval where we observe the development of a network of Riedel shear surfaces.

5. Conclusions

We document the evolution of fabric elements in clay rich fault gouge as a function of shear strain, clay mineralogy, and particle morphology. Fabric elements develop systematically with shear strain, beginning with R_1 shears developing at the yield stress and propagating through the layer. The Riedel shears nucleate at the layer margins and propagate into the layer; Riedel shears cross the layer by shear strains of ~ 1–2 beyond the yield stress. As multiple Riedel shears transect the layer, clay particles begin to rotate to the P orientation, with their long axes are perpendicular to σ_1. SEM observations indicate Riedel shears in clay are narrow and smooth, unlike in other granular materials. Individual Riedel surfaces and associated damage zones are only a few microns thick, with surface areas of up to several square centimetres.

Clay fabric measurements indicate that the rotation of clay particles into the P orientation is dictated primarily by shear strain, but that the intensity of preferred phyllosilicate orientation is controlled primarily by particle morphology. Acoustic wave velocities are sensitive to both the application of load, and the formation and propagation of shear surfaces. Acoustic measurements may prove useful as probes of fabric development in future experiments, because changes in acoustic velocities can be linked to the growth and propagation of specific fabric elements. Our work indicates that clay-rich materials may be very weak without significant cataclasis, and that arguments for the nature of the frictional weakness of clays based on a highly anisotropic clay mineral structure may not be valid. Instead, we suggest that a combination of fine grain size and a polymodal particle size distribution permits strain accommodation primarily along very narrow surfaces with only limited cataclasis.

Acknowledgements

We are grateful to Toshikito Shimamoto for a thoughtful review that significantly improved the manuscript, and to Tom Blenkinsop for editorial review. We are grateful to Anja Schleicher and Carl Henderson for maintenance of the EMAL facility at the University of Michigan. We thank Matt Ikari for use of experimental data. This work was supported by NSF grants OCE-0648331, EAR-0746192, and EAR-0950517 to Saffer and Marone, and grants EAR-0738435 and EAR-1118704 to van der Pluijm for support of XTG facilities. A grant from the GDL Foundation to Haines is also gratefully acknowledged.

References

Anthony, J., Marone, C., 2005. Influence of particle characteristics on granular friction. J. Geophys. Res. 110, B08409. http://dx.doi.org/10.1029/2004JB003399.
Arch, J., Maltman, A., Knipe, R., 1988. Shear-zone geometry in experimentally-deformed clays: the influence of water content, strain rate and primary fabric. J. Struct. Geol. 10, 91–99.
Beeler, N., Tullis, T., Blanpied, M., Weeks, J., 1996. Frictional behavior of large displacement experimental faults. J. Geophys. Res. 101, 8697–8715.
Bird, P., 1984. Hydration-phase diagrams and friction of montmorillonite under laboratory and geologic conditions, with implications for shale compaction, slope stability, and strength of fault gouge. Tectonophysics 107, 235–260.
Brown, K., Bekins, B., Clennell, B., Dewhurst, D., Westbrook, G., 1994. Heterogeneous hydrofracture development and accretionary fault dynamics. Geology 22, 259–262.
Byerlee, J., 1978. Friction of rocks. Pure Appl. Geophys. 116, 615–626.
Carpenter, B., Marone, C., Saffer, D., 2011. Weakness of the San Andreas Fault revealed by samples from the active fault zone. Nat. Geosci. 4, 251–254.
Chester, F., Logan, J., 1987. Composite planar fabric of gouge from the Punchbowl Fault, California. J. Struct. Geol. 9, 621–634.

Cladouhos, T., 1999a. Shape preferred orientations of survivor grains in fault gouge. J. Struct. Geol. 21, 419–436.
Cladouhos, T., 1999b. A kinematic model for deformation within brittle shear zones. J. Struct. Geol. 21, 437–448.
Cloos, H., 1928. Experimente zur inneren Tectonik. Centeralbl. Mineral. Geol. U Pal. 1929B, 609–621.
Collettini, C., Niemeijer, A., Viti, C., Marone, C., 2009. Fault zone fabric and fault weakness. Nature 462, 907–910. http://dx.doi.org/10.1038/nature08585.
Collettini, C., Niemeijer, A., Viti, C., Smith, S., Marone, C., 2011. Fault structure, frictional properties and mixed-mode fault slip behavior. Earth Planetary Sci. Lett. 311, 316–327. http://dx.doi.org/10.1016/j.epsl.2011.09.020.
Colten-Bradley, V., 1987. Role of pressure in smectite dehydration–effects on geopressure and smectite-to-illite transformation. AAPG Bull. 71, 1414–1427.
Cowan, D., 1999. Do faults preserve a record of seismic slip? A field geologist's opinion. J. Struct. Geol. 21, 995–1001.
Cowan, D., Cladouhos, T., Morgan, J., 2003. Structural geology and kinematic history of rocks formed along low-angle normal faults, Death Valley, California. Geol. Soc. Am. Bull. 115, 1230–1248.
Crawford, B., Faulkner, D., Rutter, E., 2008. Strength, porosity, and permeability development during hydrostatic and shear loading of synthetic quartz-clay fault gouge. J. Geophys. Res. B 113. http://dx.doi.org/10.1029/2006JB004634.
Day-Stirrat, R., Schleicher, A., Schneider, J., Flemings, P., Germaine, J., van der Pluijm, B., 2011. J. Struct. Geol. 33, 1347–1358.
Dieterich, J., 1981. Constitutive properties of faults with simulated gouge. In: Carter, N.L., et al. (Eds.), Mechanical Behavior of Crustal Rocks: Geophysical Monograph Series, vol. 24. AGU, Washington, D.C, pp. 102–120.
Erickson, S., Wiltschko, D., 1991. Spatially heterogeneous strength in a thrust fault zone. J. Geophys. Res. B 96, 8427–8440.
Faulkner, D., Jackson, C., Lunn, R., Schlische, R., Shipton, Z., Wibberly, C., 2010. A review of recent developments concerning the structure, mechanics and fluid flow properties of fault zones. J. Struct. Geol. 32, 1557–1575.
Faulkner, D., Rutter, E., 1998. The gas permeability of clay-bearing fault gouge at 20 °C. In: Jones, G., Fisher, Q., Knipe, R. (Eds.), Faulting, Fault Sealing and Fluid Flow in Hydrocarbon Reservoirs. Geol. Soc. London Special Publication 147, pp. 147–156.
Fortin, J., Schubnel, A., Gueguen, Y., 2005. Elastic wave velocities and permeability evolution during compaction of Bleurswiller sandstone. Int. J. Rock Mechanics Mining Sci. 42, 873–889.
Fortin, J., Gueguen, Y., Schubnel, A., 2007. Effects of pore collapse and grain crushing on ultrasonic velocities and V_p/V_s. J. Geophys. Res. B 112. http://dx.doi.org/10.1029/2005JGB004005.
Gilbert, G., 1884. A theory of the earthquakes of the Great Basin, with a practical application. Am. J. Sci. XXVII, 49–54.
Haines, S, 2008. Transformations in Clay-rich Fault Rocks: Constraining Fault Zone Processes and the Kinematic Evolution of Regions. Unpublished Ph.D. thesis, Univ. Michigan, Ann. Arbor, 295 pp.
Haines, S., van der Pluijm, B., Ikari, M., Saffer, D., Marone, C., 2009. Clay fabric intensity in natural and artificial fault gouges: Implications for brittle fault zone processes and sedimentary basin clay fabric evolution. J. Geophys. Res. B 114. http://dx.doi.org/10.1029/2008JB005866.
Haines, S., van der Pluijm, B., 2012. Patterns of mineral transformations in clay gouge, with examples from low-angle normal fault rocks in the western USA. J. Struct. Geol. 43, 2–32.
Hayman, N., 2006. Shallow crustal faults from the Black Mountain detachments, Death Valley, CA. J. Struct. Geol. 28, 1767–1784.
Ikari, M., Saffer, D., Marone, C., 2007. Effect of hydration state on the frictional properties of montmorillonite-based fault gouge. J. Geophys. Res. B 112. http://dx.doi.org/10.1029/2006JB004748.
Ikari, M., Saffer, D., Marone, C., 2009. Frictional and hydrologic properties of clay-rich fault gouge. J. Geophys. Res. B 114. http://dx.doi.org/10.1029/2008JB006089.
Ikari, M., Marone, C., Saffer, D., 2011. On the relation between fault strength and frictional stability. Geology 39, 83–86.
Ikari, M., Saffer, D., 2011. Comparison of frictional strength and velocity dependence between fault zones in the Nankai accretionary complex. Geochem. Geophys. Geosyst.. http://dx.doi.org/10.1029/2010GC003442
Knuth, M., 2011. Ultrasonic Velocity Measurements in Sheared Granular Layers: Implications for the Evolution of Dynamic Elastic Moduli of Compositionally-diverse Cataclastic Fault Gouges. Unpublished Ph.D. thesis, The University of Wisconson, Madison. 137 pp.
Logan, J., Rauenzahn, K., 1987. Frictional dependence of gouge mixtures of quartz and montmorillonite on velocity, composition and fabric. Tectonophysics 144, 87–108.
Logan, J., Freidman, M., Higgs, M., Dengo, C., Shimamoto, T., 1979. Experimental studies of simulated fault gouge and their application to studies of natural fault zones. In: Proc. Conf. VIII, Analysis of Actual Fault Zones in Bedrock. U.S. Geological Survey, Menlo Park, CA, pp. 305–343.
Logan, J., Dengo, C., Higgs, N., Wang, Z.-Z., 1992. Fabrics of experimental fault zones: their development and relationship to mechanical behavior. In: Fault Mechanics and Transport Properties of Rocks, 51. Academic Press, pp. 33–67.
Mair, K., Marone, C., 1999. Friction of simulated fault gouge for a wide range of velocities and normal stresses. J. Geophys. Res. B 104, 28,899–29,914.
Maltman, A., 1977. Some microstructures of experimentally deformed argillaceous sediments. Tectonophysics 39, 417–436.
Maltman, A., 1987. Shear zones in argillaceous sediments – an experimental study. In: Jones, M., Preston, R. (Eds.), Deformation of Sediments and Sedimentary Rocks. Geol. Soc. London Special Pub. 29, pp. 77–87.
Marone, C., Raleigh, B., Scholz, C., 1990. Frictional behavior and constitutive modeling of simulated fault gouge. J. Geophys. Res. 95, 7007–7025.
Marone, C., Scholz, C., 1989. Particle-size distribution and microstructures within simulated fault gouge. J. Struct. Geol. 11, 799–814.
Miller, M., 1996. Ductility in fault gouge from a normal fault system, Death Valley, California: a mechanism for fault zone strengthening and relevance to paleoseismicity. Geology 24, 603–606.
Moore, D., Summers, R., Byerlee, J., 1989. Sliding behavior and deformation textures of heated illite gouge. J. Struct. Geol. 11, 329–342.
Moore, D., Lockner, D., 2004. Crystallographic controls on the frictional behavior of dry and water-saturated sheet structure minerals. J. Geophys. Res. B 109, B03401. http://dx.doi.org/10.1029/2003JB002582.
Moore, D., Reynolds, R., 1997. X-ray Diffraction and the Identification and Analysis of Clay Minerals. Oxford University Press, New York, 378 pp.
Morgenstern, N., Tchalenko, J., 1967. Microscopic structures in kaolin subject to direct shear. Géotechnique 17, 309–328.
Morrow, C., Shi, L.Q., Byerlee, J., 1984. Permeability of fault gouge under confining pressure and shear stress. J. Geophys. Res. B 89, 3193–3200.
Morrow, C., Radney, B., Byerlee, J., 1992. Frictional strength and the effective pressure law of montmorillonite and illite clays. In: Evans, B., Wong, T.-F. (Eds.), Fault Mechanics and Transport Properties of Rocks, pp. 69–88.
Morrow, C., Moore, D., Lockner, D., 2000. The effect of mineral bond strength and adsorbed water on fault gouge frictional strength. Geophys. Res. Lett. 27, 815–818.
Naylor, M., Mandl, G., Sijpsteijn, C., 1986. Fault geometries in basement-induced wrench faulting under different initial stress states. J. Struct. Geol. 8, 737–752.
Niemeijer, A., Spiers, C., 2007. A microphysical model for strong velocity weakening in phyllosilicate-bearing fault gouges. J. Geophys. Res. B 112. http://dx.doi.org/10.1029/2007JB005008.
Niemeijer, A., Marone, C., Elsworth, D., 2010a. Fabric induced weakness of tectonic faults. Geophys. Res. Lett. 37, L03304. http://dx.doi.org/10.1029/2009GL041689.
Niemeijer, A., Marone, C., Elsworth, D., 2010b. Frictional strength and strain weakening in simulated fault gouge: competition between geometrical weakening and chemical strengthening. J. Geophys. Res. B 115, B10207. http://dx.doi.org/10.1029/2009JB000838.
Niemeijer, A., Di Toro, G., Nielsen, S., Di Felice, F., 2010c. Frictional melting of gabbro under extreme experimental conditions of normal stress, acceleration and sliding velocity. J. Geophyical. Res. B. http://dx.doi.org/10.1029/2010JB008181.
Pavlis, T., Serpa, L., Keener, C., 1993. Role of seismogenic processes in fault-rock development; an example from Death Valley, California. Geology 21, 267–270.
Popp, T., Salzer, K., 2007. Anisotropy of seismic and mechanical properties of Opalinus clay during triaxial deformation in a multi-anvil apparatus. Phys. Chem. Earth 32, 879–888.
Riedel, W., 1929. Zur mechanik geologisher Brucherscheinungen. Centralbl. Mineral. Geol. U Pal. 1929B, 354–368.
Rutter, E., Maddock, R., Hall, S., White, S., 1986. Comparative microstructures of naturally and experimentally produced clay-bearing fault gouges. Pure Appl. Geophys. 124, 3–30.
Saffer, D., Frye, K., Marone, C., Mair, K., 2001. Laboratory results indicating weak and potentially unstable frictional behavior of smectite clay. Geophys. Res. Lett. 28, 2,297–2,300.
Saffer, D., Marone, C., 2003. Comparison of smectite- and illite-rich gouge frictional properties: application to the updip limit of the seismogenic zone along subduction megathrusts. Earth Planetary Sci. Lett. 215, 219–235.
Sayers, C., Kachanov, M., 1995. Microcrack-induced elastic wave anisotropy of brittle rocks. J. Geophys. Res. B 100, 4149–4156.
Schleicher, A., van der Pluijm, B., Solum, J., Warr, L., 2006. Origin and significance of clay-coated fractures in mudrock fragments of the SAFOD borehole (Parkfield California). Geophys. Res. Lett. 33, L16313. http://dx.doi.org/10.1029/2006GL026505.
Schleicher, A., van der Pluijm, B., Warr, L., 2010. Nano-coatings of clay control creep and strength along the San Andreas Fault at Parkfield, California. Geology 38, 667–670.
Schubnel, A., Fortin, J., Burlini, L., Gueguen, Y., 2005. Damage and recovery of calcite rocks deformed in the cataclastic regime. In: Bruhn, D., Burlini, L. (Eds.), High-strain Zones: Structure and Physical Properties. Geol. Soc. London Spec. Pub. 245, pp. 203–221.
Scholz, C., 2002. The Mechanics of Earthquakes and Faulting, second ed. Cambridge Press, New York, NY.
Scott, D., Marone, C., Sammis, C., 1994. The apparent friction of granular fault gouge in sheared layers. J. Geophys. Res. B 99, 7231–7247.
Shimamoto, T., Logan, J., 1981. Effects of simulated clay gouges on the sliding behavior of Tennessee sandstone. Tectonophysics 75, 243–255.
Shimamoto, T., Tsutsumi, A., 1994. A new rotary-shear high-speed frictional testing machine: its basic design and scope of research. J. Tecton. Res. Group Jpn. 39, 65–78 (in Japanese with English abstract).
Sibson, R., 1977. Fault rocks and fault mechanisms. J. Geol. Soc. London 133, 191–213.
Sintubin, M., Wenk, H.-R., Phillips, D., 1995. Texture development in platy materials: comparison of Bi2223 aggregates with phyllosilicate fabrics. Mater. Sci. Eng. A202, 157–171.

Storti, F., Balsamo, F., 2010. Impact of ephemeral cataclastic fabrics on laser diffraction particle size distribution analysis in loose carbonate fault breccia. J. Struct. Geol. 32, 507–522.
Summers, R., Byerlee, 1977. A note on the effect of fault gouge composition on the stability of frictional sliding. Int. J. Rock Mechanics Mining Sci. 14, 155–160.
Takahashi, M., Mizoguchi, K., Kitamura, K., Masuda, K., 2007. Effects of clay content on the frictional sliding of granite. J. Geophys. Res. B 112, B08206. http://dx.doi.org/10.1029/2006JB004678.
Tchalenko, J., 1968. The evolution of kink-bands and the development of compression textures in sheared clays. Tectonophysics 6, 159–174.
Tchalenko, J., 1970. Similarities between shear zones of different magnitudes. Geol. Soc. Am. Bull. 81, 1625–1640.
Tembe, S., Lockner, D., Wong, T.-F., 2010. Effect of clay content and mineralogy on frictional sliding behavior of simulated gouges: binary and ternery mixtures of quartz, illite and montmorillonite. J. Geophys. Res. B 115, B03416. http://dx.doi.org/10.1029/2009JB006383.
van der Pluijm, B., Ho, N.-C., Peacor, D., 1994. High-resolution X-ray texture goniometry. J. Struct. Geol. 16, 1029–1032.
Vannucchi, P., Maltman, A., Bettelli, G., Clennell, B., 2003. On the nature of scaly fabric and scaly clay. J. Struct. Geol. 25, 673–688.
Wang, C.-Y., Mao, W.-H., Wu, F., 1980. Mechanical properties of clays at high pressure. J. Geophys. Res. B 85, 1462–1468.
Weber, K., Mandl, G., Pilaar, W., Lehner, F., Precious, R., 1978. The role of faults in hydrocarbon migration and trapping in Nigerian growth fault structures. In: Proceedings 10th Annual Offshore Technology Conference, OTC 3556, pp. 2643–2647.
Wenk, H., 1985. Measurements of pole figures. In: Wenk, H. (Ed.), Preferred Orientation in Deformed Metals and Rocks. Academic Press, Orlando, pp. 11–47.
Wijeyesekera, D., de Freitas, M., 1976. High-pressure consolidation of kaolinitic clay. Am. Assoc. Pet. Geol. Bull. 60, 293–298.
Wu, F., 1978. Mineralogy and physical nature of fault gouge. Pure Appl. Geophys. 116, 655–689.
Wu, T., Blatter, L., Roberson, H., 1975. Clay gouges in the San Andreas Fault System and their possible implications. Pure Appl. Geophys. 113, 87–95.